THE CASSINI RADIO AND PLASMA WAVE INVESTIGATION

D. A. GURNETT,[1,*] W. S. KURTH,[1] D. L. KIRCHNER,[1] G. B. HOSPODARSKY,[1]
T. F. AVERKAMP,[1] P. ZARKA,[2] A. LECACHEUX,[2] R. MANNING,[2,†] A. ROUX,[3]
P. CANU,[3] N. CORNILLEAU-WEHRLIN,[3] P. GALOPEAU,[3] A. MEYER,[3]
R. BOSTRÖM,[4] G. GUSTAFSSON,[4] J.-E. WAHLUND,[4] L. ÅHLEN,[4] H. O. RUCKER,[5]
H. P. LADREITER,[5] W. MACHER,[5] L. J. C. WOOLLISCROFT,[6,†] H. ALLEYNE,[6]
M. L. KAISER,[7] M. D. DESCH,[7] W. M. FARRELL,[7] C. C. HARVEY,[8] P. LOUARN,[8]
P. J. KELLOGG,[9] K. GOETZ[9] and A. PEDERSEN[10]

[1]*Department of Physics and Astronomy, University of Iowa, Iowa City, IA 52242, U.S.A.*
[2]*Observatoire de Paris, Meudon, France*
[3]*CETP/UVSQ, Velizy, France*
[4]*Swedish Institute of Space Physics, Uppsala, Sweden*
[5]*Austrian Academy of Sciences, Space Research Institute, Graz, Austria*
[6]*Department of Automatic Control and Systems Engineering, University of Sheffield, Sheffield, U.K.*
[7]*NASA/Goddard Space Flight Center, Greenbelt, MD 20771, U.S.A.*
[8]*CESR/CNRS, Toulouse, France*
[9]*Department of Physics and Astronomy, University of Minnesota, Minneapolis, MN 55455, U.S.A.*
[10]*Department of Physics, University of Oslo, Blindern, Oslo, Norway*
*(*Author for correspondence: E-mail address: donald-gurnett@uiowa.edu)*

(Received 11 June 1998; Accepted in final form 5 September 2002)

Abstract. The Cassini radio and plasma wave investigation is designed to study radio emissions, plasma waves, thermal plasma, and dust in the vicinity of Saturn. Three nearly orthogonal electric field antennas are used to detect electric fields over a frequency range from 1 Hz to 16 MHz, and three orthogonal search coil magnetic antennas are used to detect magnetic fields over a frequency range from 1 Hz to 12 kHz. A Langmuir probe is used to measure the electron density and temperature. Signals from the electric and magnetic antennas are processed by five receiver systems: a high frequency receiver that covers the frequency range from 3.5 kHz to 16 MHz, a medium frequency receiver that covers the frequency range from 24 Hz to 12 kHz, a low frequency receiver that covers the frequency range from 1 Hz to 26 Hz, a five-channel waveform receiver that covers the frequency range from 1 Hz to 2.5 kHz in two bands, 1 Hz to 26 Hz and 3 Hz to 2.5 kHz, and a wideband receiver that has two frequency bands, 60 Hz to 10.5 kHz and 800 Hz to 75 kHz. In addition, a sounder transmitter can be used to stimulate plasma resonances over a frequency range from 3.6 kHz to 115.2 kHz. Fluxes of micron-sized dust particles can be counted and approximate masses of the dust particles can be determined using the same techniques as Voyager. Compared to Voyagers 1 and 2, which are the only spacecraft that have made radio and plasma wave measurements in the vicinity of Saturn, the Cassini radio and plasma wave instrument has several new capabilities. These include (1) greatly improved sensitivity and dynamic range, (2) the ability to perform direction-finding measurements of remotely generated radio emissions and wave normal measurements of plasma waves, (3) both active and passive measurements of plasma resonances in order to give precise measurements of the local electron density, and (4) Langmuir probe measurements of the local electron density and temperature. With these new capabilities, it will be possible to perform a broad range of studies of radio emissions, wave-particle interactions, thermal plasmas and dust in the vicinity of Saturn.

[†]Deceased

Space Science Reviews **114:** 395–463, 2004.

1. Introduction

This paper describes the Cassini radio and plasma wave science investigation, hereafter referred to by the acronym RPWS. The basic objectives of the RPWS investigation are to study radio emissions, plasma waves, thermal plasma, and dust in the vicinity of Saturn. The Voyager 1 and 2 spacecraft, which made the first radio and plasma wave measurements at Saturn, clearly showed that many complex types of wave phenomena exist in Saturn's magnetosphere (Warwick *et al.*, 1981; Gurnett *et al.*, 1981; Warwick *et al.*, 1982; Scarf *et al.*, 1982). For a description of the radio and plasma wave instrumentation on Voyager see Warwick *et al.* (1977) and Scarf and Gurnett (1977), and for an overview of radio and plasma wave observations in the vicinity of Saturn see Kaiser *et al.* (1984a) and Scarf *et al.* (1984). The Cassini RPWS instrument is considerably more complex and has greatly improved capabilities compared to the Voyager radio and plasma wave instruments. Voyager used two orthogonal 10-m electric antennas for electric field measurements. The radio instrument used these antennas as two independent monopoles (for both intensity and limited polarization measurements) and the plasma wave instrument used them as a single-axis dipole. In contrast, the Cassini RPWS uses three nearly orthogonal 10-m electric antennas for electric field measurements, three orthogonal search coil magnetometers for magnetic field measurements, and a Langmuir probe for electron density and temperature measurements. Electric field measurements are made over a frequency range from 1 Hz to 16 MHz, magnetic field measurements are made over a frequency range from 1 Hz to 12 kHz, and electron density fluctuation measurements are made over a frequency range from 1 Hz to 2.5 kHz. Signals from the electric and magnetic antennas are processed by five on-board receivers, all considerably more advanced than those flown on Voyager. These include a high frequency digital spectrum analyzer to perform high frequency (3.5 kHz to 16 MHz) spectral, polarization, and direction-finding measurements, a medium frequency analog receiver to perform medium-frequency (24 Hz to 12 kHz) spectral measurements, a low frequency (1 Hz to 26 Hz) digital receiver to perform low frequency spectral measurements, a five-channel waveform receiver to perform wave normal and fine-scale plasma structure measurements, and a digital wideband receiver to provide high-resolution frequency-time spectrograms. In addition, a sounder transmitter can be used to excite local plasma resonances, and a Langmuir probe is used to provide measurements of the electron density and temperature. As with Voyager (Gurnett *et al.*, 1983; Aubier *et al.*, 1983), the RPWS will be able to measure the flux of dust and make estimates of the mass of the dust particles from the signature of impacts with the spacecraft.

Since the Cassini spacecraft is to be the first orbiter of Saturn, this spacecraft will provide much better spatial and temporal coverage than was possible with Voyagers 1 and 2. Specifically, the orbit of Cassini is expected to provide equatorial coverage of all local times for radial distances ranging from about 3.1 R_S

(Saturn radii) to more than 60 R_S. This spatial coverage will provide numerous passes through the bow shock, the magnetopause, the outer magnetosphere, and the inner magnetosphere. During a latter phase of the mission, the inclination of the orbit will be increased to about 75°, thereby providing coverage of the magnetosphere at high latitudes in the vicinity of the auroral field lines. In addition to the magnetospheric coverage, the spacecraft will provide more than 44 close flybys of Saturn's large moon Titan, and close flybys of Saturn's small icy satellites (Mimas, Enceladus, Tethys, Dione, and Rhea). A prime objective of these flybys will be to study the plasma environment of the moons and their interaction with the magnetosphere of Saturn. The flybys of Titan are of particular interest, since Titan is known to have a dense atmosphere (Hunten *et al.*, 1984) and acts as a major source of plasma in the outer regions of the magnetosphere (Neubauer *et al.*, 1984). The small icy moons, Enceladus and Dione in particular, are suspected to be a source of plasma in the inner magnetosphere (Scarf *et al.*, 1984). For an overview of the scientific objectives of the Cassini mission see Matson *et al.* (this issue). For a review of the magnetospheric objectives for the mission, see Blanc *et al.* (2002).

The RPWS investigation is a multi-institutional effort involving 22 investigators from 6 countries and 10 institutions. A list of the investigators, their affiliation and their responsibilities is given in Table I. The investigation is led by Donald A. Gurnett of the University of Iowa, who is the Principal Investigator. The Deputy Principal Investigator is William S. Kurth. During the hardware phase the Project Manager was Richard L. Huff, and the Principal Engineer was Donald L. Kirchner, all at the University of Iowa. Four institutions produced hardware for the project: the University of Iowa, the Observatoire de Paris, the Centre d'etudes des Environnements Terrestre et Planetaires (Universite Versailles Saint Quentin), and the Swedish Institute of Space Physics. The University of Sheffield developed various parts of the flight software, and the Space Research Institute of the Austrian Academy of Sciences carried out radiation pattern studies of the electric antennas. The scientific objectives of the investigation, a description of the instrument, and a discussion of the in-flight operations and data analysis are given in the following sections, which are organized as follows. Section 2 discusses the scientific objectives, Section 3 describes the instrumentation requirements needed to achieve the scientific objectives, Section 4 describes the instrumentation, Section 5 describes the calibrations and performance, and Section 6 describes the in-flight operations, data analysis and data archiving.

2. Scientific Objectives

The scientific objectives of the Cassini RPWS investigation can be broken down into five topics: radio emissions, plasma waves, lightning, thermal plasma, and dust, each of which is discussed below.

TABLE I
RPWS investigators.

RPWS investigator	Institution (Country)	Main responsibility
D. A. Gurnett (P.I.) and W. S. Kurth (Deputy P.I.)	University of Iowa (USA)	Data processing unit. Medium frequency receiver. Wideband receiver; Waveform receiver. Electric antenna motor driver. Electric antenna procurement. Data analysis.
A. Lecacheux and P. Zarka	Observatoire de Paris (France)	High frequency receiver. Sounder; Power supply. Electric preamplifiers. Electric antenna procurement. Data analysis.
P. Canu, N. Cornilleau-Wehrlin, P. Galopeau and A. Roux	CETP/UVSQ (France)	Magnetic antennas. Data analysis.
R. Boström, G. Gustafsson and J.-E. Wahlund	Swedish Inst. of Physics (Sweden)	Langmuir probe. Langmuir probe preamplifier. Langmuir probe digital processor. Data analysis.
H. P. Ladreiter and H. O. Rucker	Austrian Academy of Sciences (Austria)	Antenna modeling. Direction-finding calibration. Data analysis.
H. Alleyne and L. J. C. Woolliscroft*	University of Sheffield (UK)	Data compression software. Data analysis.
M. D. Desch, W. M. Farrell and M. L. Kaiser	NASA/Goddard Space Flight Center (USA)	Data analysis.
C. C. Harvey and P. Louarn	CESR/CNRS (France)	Data analysis.
K. Goetz and P. J. Kellogg	University of Minnesota (USA)	Data analysis.
A. Pedersen	University of Oslo (Norway)	Data analysis.

*Deceased

2.1. Radio Emissions

It is now known that the magnetospheres of five magnetized planets, Earth, Jupiter, Saturn, Uranus, and Neptune, are sources of non-thermal radio emissions (Kaiser, 1989; Zarka, 1998). In addition, one of Jupiter's moons, Ganymede, is also known to produce non-thermal radio emissions (Gurnett *et al.*, 1996; Kurth *et al.*, 1997). These magnetospheric radio emissions are important not only because of the basic plasma processes involved, but also because they provide a valuable remote sensing tool. Since the beaming pattern of the radio emission source is in all cases strongly controlled by the large-scale magnetic field of the planet, the modulation of the radio emission intensity as the planet rotates provides a direct link with the deep interior of the planet. At the present time the only method of accurately determining

the rotation rate of the interior of the outer planets is by monitoring the rotational modulation of magnetospheric radio emissions.

Although various radio emission mechanisms have been identified in planetary magnetospheres, one mechanism stands out above all others in terms of radiated power: the cyclotron maser mechanism (Wu and Lee, 1979). Cyclotron maser radiation is produced by a coherent electromagnetic plasma instability and is generated at frequencies very close to the electron cyclotron frequency, which is the frequency of an electron's cyclotron motion in a magnetic field. The electron cyclotron frequency is given by $f_{ce} = 28\text{B}$ Hz, where B is the magnetic field strength in nT (Stix, 1992). Since the coupling in the cyclotron maser mechanism is with the electrons, the radiation is primarily right-hand polarized with respect to the magnetic field (i.e., the electric field vector rotates in the same sense as the cyclotron motion of an electron). At Earth, cyclotron maser radiation is closely associated with discrete auroral arcs (Gurnett, 1974) and is often called auroral kilometric radiation (AKR). The free energy source responsible for the cyclotron maser radiation was originally believed to be a loss-cone anisotropy in the auroral electron distribution (Wu and Lee, 1979; Le Queau *et al.*, 1984). However, more recent measurements suggest that the free energy source is either due to a ring distribution (Louarn *et al.*, 1990) formed by electrons that are electrostatically trapped by the magnetic mirror force of the planetary magnetic field and the parallel electric field responsible for the auroral electron acceleration, or by a shell distribution (Ergun *et al.*, 2000) formed by the acceleration due to the parallel electric field. For a discussion of the cyclotron maser instability and its application to planetary radio emission, see Zarka (1998). In addition to the cyclotron maser radiation, several other considerably weaker radio emission mechanisms have also been identified in planetary magnetospheres. These include synchrotron radiation (Carr *et al.*, 1983), mode conversion from electrostatic upper hybrid waves (Jones, 1976), and mode conversion from Langmuir waves (Cairns and Melrose, 1985). For a review of these and various other radio emission mechanisms, see Goldstein and Goertz (1983) and Zarka (1998).

Most of our present knowledge of radio emissions from Saturn's magnetosphere comes from Voyagers 1 and 2 (Warwick *et al.*, 1981, 1982; Gurnett *et al.*, 1981; Scarf *et al.*, 1982). The Voyager measurements show that the radio emission spectrum of Saturn extends over a very broad frequency range, from about 3 kHz to 1.2 MHz, and has a broad peak extending from about 100–400 kHz. Since the peak intensity occurs at kilometer wavelengths, this radiation is called Saturn kilometric radiation (SKR). The intensity and shape of the SKR spectrum is shown in Figure 1, and is very similar to terrestrial AKR. The total radiated power ranges from about 10^8–10^{10} Watts, and the radiation is generated near the local electron cyclotron frequency primarily in the right-hand polarized extraordinary mode. Because of the characteristic frequency and polarization, it is now widely believed that SKR is generated by the cyclotron maser mechanism (Galopeau *et al.*, 1989). Studies of the radiation pattern (Kaiser *et al.*, 1981; Kaiser and Desch, 1982; Lecacheux and Genova, 1983) indicate that the radiation is generated over the dayside auroral

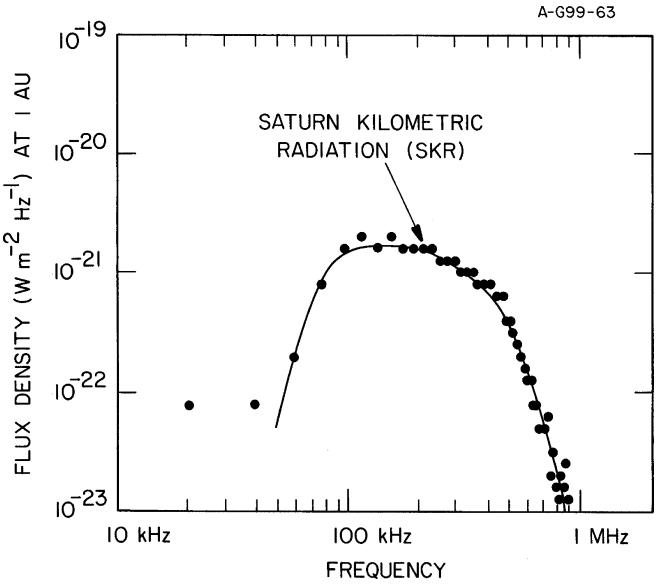

Figure 1. A typical spectrum of Saturn kilometric radiation, which is an intense radio emission that occurs in a frequency range from about 100 to 800 kHz. This radio emission is believed to be generated at low altitudes in the dayside auroral regions by the cyclotron maser mechanism. The intensities have been normalized to a radial distance of 1 AU (astronomical unit).

zone on magnetic field lines that pass through or near the dayside polar cusps. The inferred source field lines projected down to the cloud tops of Saturn are shown in Figure 2 (from Galopeau *et al.*, 1995). These projected source locations are in good agreement with the location of Saturn's aurora from the Hubble Space Telescope (Trauger *et al.*, 1998). Our present knowledge of the rotational period of Saturn (10 h 39.4 min) comes almost entirely from the rotational modulation of SKR (Desch and Kaiser, 1981). One surprising and still unexplained feature is that a strong rotational modulation occurs even though the magnetic dipole axis of Saturn is aligned within 1° of the rotational axis. Most likely the magnetic field of Saturn has significant deviations from a dipole field near the planet (Galopeau *et al.*, 1991; Galopeau and Zarka, 1992). Also, there is evidence of long-term variations in the SKR period that may ultimately limit the accuracy with which the rotational period of Saturn can be determined (Lecacheux *et al.*, 1997; Galopeau and Lecacheux, 2000; Zarka and Cecconi, 2002).

In addition to the rotational modulation, the SKR intensity also displays considerable variability on time scales ranging from seconds to months. Studies by Desch (1982) show that the SKR intensity is strongly influenced by solar wind pressure variations. Higher SKR intensities are associated with higher solar wind pressures. Kurth *et al.* (1981) have also shown that the orbital position of Saturn's large icy moon Dione may play a role in modulating the SKR intensity, possibly suggesting an Alfvén wave-like interaction with the magnetosphere of Saturn, similar to

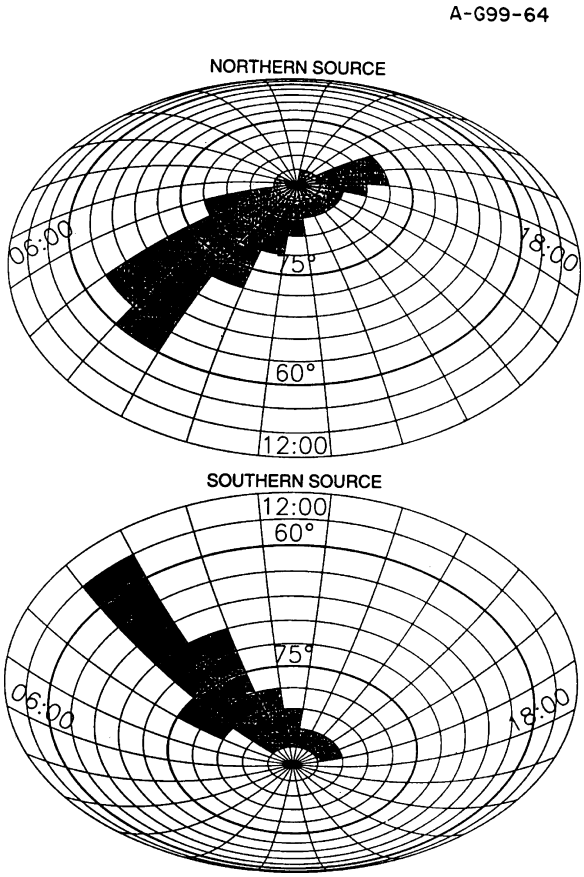

Figure 2. SKR source locations projected down Saturn's magnetic field lines to the cloud tops (from Galopeau *et al.*, 1995). These source positions are in good agreement with the location of Saturn's aurora, as determined from ultraviolet images taken by the Hubble Space Telescope (Trauger *et al.*, 1998).

the interaction of Jupiter's moon Io with the magnetosphere of Jupiter (Goldreich and Lynden-Bell, 1969). For a discussion of the Alfvén wave interaction at Io, see Neubauer (1980). It has long been suspected that gaseous emissions from Dione and various other icy moons of Saturn, such as Enceladus and Tethys, are significant sources of plasma in the inner regions of the magnetosphere. Therefore, these moons could very well induce an Alfvén wave interaction similar to the interaction that occurs at Io. Evidence also exists that the occurrence of SKR is linked with the occurrence of spokes in the rings (Mendis *et al.*, 1984). Zarka (1998) has also shown that the SKR has considerable fine structure on time scales of a fraction of a second or less, possibly similar to the fine structure observed in terrestrial AKR (Gurnett *et al.*, 1979a). For a more detailed review of the Voyager SKR observations and their interpretation, see Kaiser *et al.* (1984a) and Zarka (1998).

In addition to the SKR, numerous other much weaker radio emissions were observed by Voyagers 1 and 2 at somewhat lower frequencies, ranging from a few kHz to several tens of kHz (Gurnett *et al.*, 1981). These emissions have very narrow bandwidths and are believed to be produced by mode conversion from electrostatic upper hybrid waves near half-integral harmonics of the electron cyclotron frequency, similar to various types of narrowband emissions observed in the magnetospheres of Earth and Jupiter (Kurth and Gurnett, 1991). The basic condition for the generation of these narrowband emissions is that the upper hybrid resonance frequency, f_{UHR}, must be near a half-integral harmonic of the electron cyclotron frequency, $(n + 1/2)f_{\mathrm{ce}}$. The upper hybrid resonance frequency is given by $f_{\mathrm{UHR}} = \sqrt{f_{\mathrm{ce}}^2 + f_{\mathrm{pe}}^2}$, where $f_{\mathrm{pe}} = 8980\sqrt{n_{\mathrm{e}}}$ Hz is the electron plasma frequency and n_e is the electron density in cm^{-3} (Stix, 1992). The frequencies of some of these emissions appear to correspond closely with half-integral harmonics of the electron cyclotron frequency near the orbits of the moons Tethys, Dione and Rhea. This relationship suggests that these moons are somehow directly involved in the generation of radio emissions, possibly by the ejection of gas that is subsequently ionized and converted to an unstable velocity distribution by an interaction with the co-rotating magnetospheric plasma. At even lower frequencies, the Voyager data suggest that electromagnetic radiation is trapped in the magnetospheric cavity at frequencies below the solar wind electron plasma frequency, very similar to continuum radiation trapped in the magnetospheres of Earth and Jupiter (Kurth, 1992). Since the low frequency cutoff of the trapped continuum radiation is usually at the local electron plasma frequency (Gurnett and Shaw, 1973; Scarf *et al.*, 1979), this cutoff could potentially provide a very accurate measurement of the local electron density, which is a basic plasma parameter of the magnetospheric plasma.

It is clear that our knowledge of radio emissions in the magnetosphere of Saturn is incomplete. Much more observing time and spatial coverage in the vicinity of Saturn are needed to fully understand the modulation effects imposed by planetary rotation, solar wind pressure variations, and interactions with Saturn's moons and rings. Direction-finding and polarization measurements are needed to constrain the generation mechanisms and to compare the source locations with other in-situ and remote sensing observations. High-time resolution measurements are needed to study the fine structure of SKR. The Cassini mission with its four years of in-orbit observations and its advanced radio wave instrumentation provides an ideal opportunity to carry out these studies. With the Cassini RPWS we expect to achieve the following specific results relative to radio emissions from Saturn's magnetosphere.

- Improve our knowledge of the rotational modulation of Saturn's radio sources, and hence of Saturn's rotation rate.
- Determine the location of the SKR source as a function of frequency, and investigate the mechanisms involved in generating the radiation.
- Obtain a quantitative evaluation of the anomalies in Saturn's magnetic field by performing direction-finding measurements of the SKR source.

- Establish if gaseous ejections from the moons Rhea, Dione, and Tethys are responsible for the low frequency narrow-band radio emissions.
- Determine if SKR is controlled by Dione's orbital position.
- Establish the nature of the solar wind-magnetosphere interaction by using SKR as a remote indicator of magnetospheric processes.
- Investigate the relationship between SKR and the occurrence of spokes and other time dependent phenomena in the rings.
- Study the fine structure in the SKR spectrum, and compare with the fine structure of terrestrial and Jovian radio emissions in order to understand the origin of this fine structure.

A recent review of some of the planetary radio astronomy issues to be addressed by Cassini at Saturn is given by Kurth and Zarka (2001).

2.2. Plasma Waves

Since plasma waves can transfer energy and momentum between particles in a plasma, plasma waves are now recognized as being of fundamental importance for understanding the dynamics of space plasmas. For example, in planetary magnetospheres, it has been known for many years (Kennel and Petschek, 1966) that wave-particle interactions play a fundamental role in controlling the loss of radiation belt particles. Charged particles trapped in a planetary magnetic field are lost if their trajectory intersects the surface or atmosphere of a planet or moon. This loss process produces a cone-shaped hole in the particle velocity distribution function called the loss cone. In the absence of plasma waves, magnetically trapped particles would bounce back and forth along the magnetic field with an essentially infinite lifetime. However, the velocity space anisotropy caused by the loss cone leads to the growth of plasma waves. In the case of electrons, the waves generated are primarily electron-cyclotron and whistler-mode waves, and in the case of ions, ion-cyclotron waves. Once generated, the waves interact resonantly with trapped particles, causing small perturbations in their trajectories relative to the magnetic field. From very general principles, it can be shown that these perturbations cause the radiation belt particles to diffuse toward the loss cone, ultimately causing the particles to be lost when they strike the planet's atmosphere (Kennel and Petschek, 1966). This loss process is the dominant mechanism that limits the lifetime of particles trapped in a planetary radiation belt. The resulting energy flux striking the atmosphere can sometimes be substantial, causing aurora and numerous other effects. In addition to radiation belt dynamics, wave-particle interactions are involved in many other processes. These include the heating of plasma at the bow shock and magnetopause, the thermalization of plasma escaping from moons and rings, and the acceleration of plasma in regions of strong field-aligned currents.

As with radio emissions, our present knowledge of plasma waves in the magnetosphere of Saturn comes almost entirely from Voyager 1 and 2 measurements

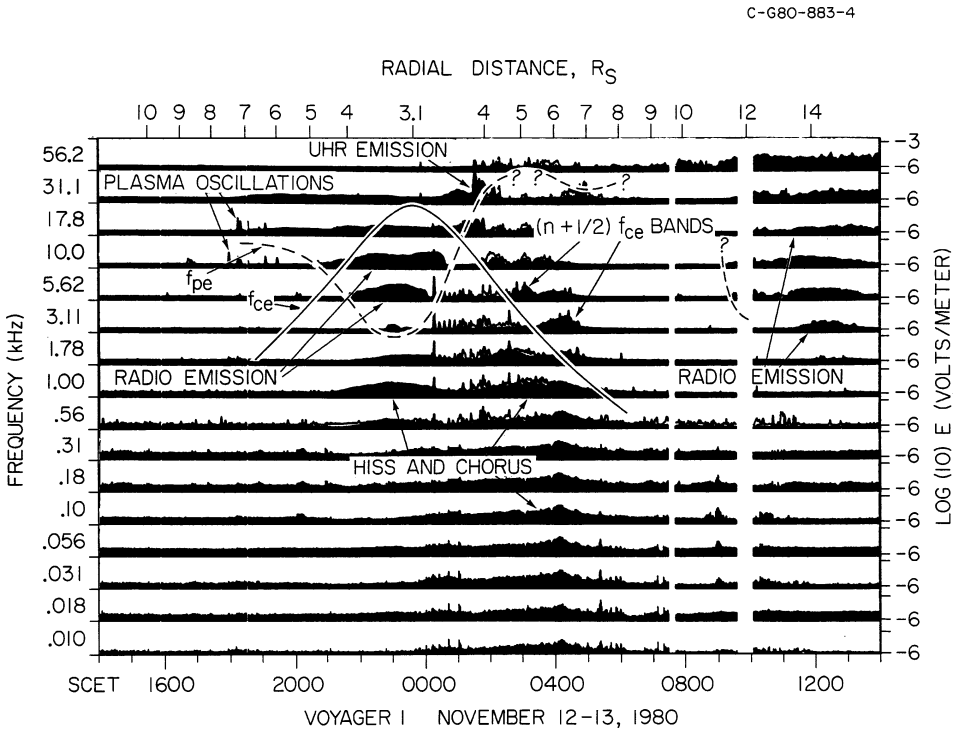

Figure 3. A 16-channel plot showing the plasma wave electric field intensities detected by the Voyager 1 plasma wave instrument during the November 12–13, 1980 flyby of Saturn (from Gurnett *et al.*, 1981). The highest plasma intensities were observed in the inner region of the magnetosphere, inside of about 10 R_S (Saturn radii).

(Gurnett *et al.*, 1981; Scarf *et al.*, 1982; Scarf *et al.*, 1984). The Voyager 1 and 2 data show that a wide variety of plasma wave phenomena are present in the magnetosphere of Saturn, and near Saturn's large moon Titan. Figure 3 gives an overview of the plasma wave electric field intensities observed during the Voyager 1 flyby of Saturn. The intensities are shown in 16 logarithmically spaced frequency channels with center frequencies extending from 10 Hz to 56.2 kHz. Spacecraft event time (SCET) in hours and minutes is shown at the bottom of the plot and the radial distance from Saturn is shown at the top of the plot in Saturn radii ($1R_s = 60{,}330$ km). As can be seen, the plasma wave phenomena occurring in the inner region of the magnetosphere are extremely complex. The plasma wave modes that can be easily identified include electron plasma oscillations, upper hybrid resonance (UHR) emissions, $(n + 1/2)f_{ce}$ electron-cyclotron waves, and whistler-mode chorus and hiss. The UHR emissions occur at the upper hybrid resonance frequency, f_{UHR}, and the electron-cyclotron waves occur near half integral harmonics of the electron cyclotron frequency, $(n + 1/2)f_{ce}$. Of these, the electron-cyclotron waves and the whistler-mode emissions are of particular importance because they control the pitch-angle scattering and loss of energetic electrons from the radiation belt.

The relatively smooth intense emissions labeled "radio emission" are the narrowband electromagnetic emissions described in the preceding section. These radio emissions are believed to be produced by mode conversion from the electrostatic UHR waves (Gurnett *et al.*, 1981). Several other types of waves are also observed that are not shown in Figure 3 . These include electrostatic waves associated with the bow shock, a broad region of low frequency MHD turbulence between the magnetopause and the rigidly co-rotating inner region of the magnetosphere, and broadband electrostatic noise in the distant magnetotail. For a detailed review of these and other types of plasma waves observed in the magnetosphere of Saturn, see Scarf *et al.* (1984).

During the Voyager 1 flyby of Saturn the spacecraft made a very close flyby of Saturn's large moon Titan, which orbits Saturn at a radial distance of about 20.2 R_S. At this large radial distance, which is near the dayside magnetopause, Titan is sometimes in the magnetosphere of Saturn and sometimes in the solar wind, depending on the solar wind pressure. During the Voyager 1 flyby, the solar wind pressure was such that Titan was inside the magnetosphere. Since the magnetosphere co-rotates with Saturn, Titan was exposed to the co-rotational plasma, which was flowing past Titan at a speed of about 120 km/s (Neubauer *et al.*, 1984). As indicated by the sketch at the top of Figure 4, the spacecraft flew almost directly through the geometric wake of Titan at a radial distance of about 2.6 Titan radii (R_T). The interaction of Titan with the rapidly flowing magnetospheric plasma produced a number of very interesting plasma wave effects. The electric field intensities from the 16-channel plasma wave spectrum analyzer are shown in Figure 4 . Two regions of intense low frequency electric field noise are evident, the first near the entry into the wake region and the second, of somewhat lower frequency, near the exit from the wake region. In the upper frequency channels, a weak narrowband emission can be seen at a frequency that has been identified as an UHR emission. Since the electron cyclotron frequency is small compared to the electron plasma frequency, the upper hybrid resonance frequency, $f_{UHR} = \sqrt{f_{ce}^2 + f_{pe}^2}$ is essentially at the electron plasma frequency. The electron density, n_e, can then be computed directly from the upper hybrid resonance frequency, and is shown by the scale on the left-hand side of the plot. As can be seen the electron density has two well-defined peaks, the first at the entry into the wake and the second at the exit from the wake. These density peaks are believed to be caused by ions escaping from Titan's ionosphere and carried downstream by the co-rotational plasma flow. The low frequency electric field noise, which occurs in the same region, is believed to be caused by a two-stream interaction between the escaping exospheric ions and the rapidly flowing magnetospheric plasma. It is believed that the waves responsible for the low frequency electric field noise play a crucial role in thermalizing and assimilating the ions from Titan's ionosphere into the magnetospheric plasma.

Although the Voyager 1 and 2 observations provide an initial overview of plasma waves in the vicinity of Saturn, much still remains to be learned. Plasma waves in the inner magnetosphere are very complex and difficult to analyze. Since very little

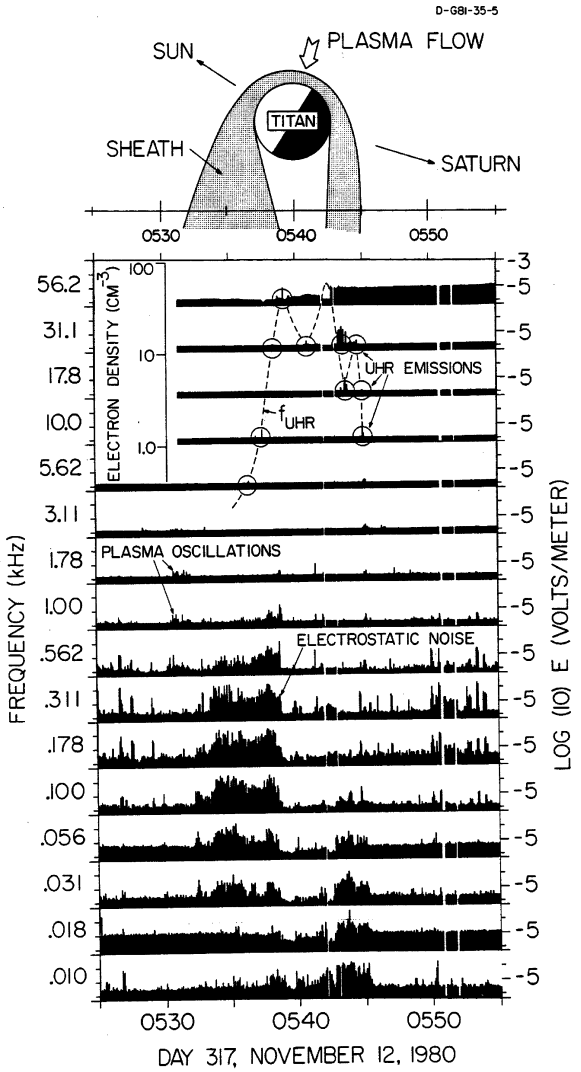

Figure 4. A 16-channel plot showing the plasma wave electric field intensities detected by the Voyager 1 plasma wave instrument during the November 12, 1980 flyby of Titan (from Gurnett *et al.*, 1981). The narrowband emission indicated by the dashed line labeled "UHR emissions" gives the local electron density, which is indicated by the scale on the left. The electron density is strongly enhanced in the region immediately downstream of Titan, indicating that plasma is being carried away from Titan by an interaction with the rapidly rotating magnetosphere of Saturn. Strong, low frequency electrostatic noise is also evident in this same region.

high-rate waveform data were obtained at Saturn, the limited frequency and time resolution of the Voyager low-rate data (as in Figures 3 and 4) makes it very difficult to distinguish various plasma wave modes. Since no wave magnetic field or density fluctuation measurements were made with the Voyager plasma wave instrument,

it is also often very difficult to distinguish electrostatic waves from electromagnetic waves, and therefore to identify the nature of the generation process. For example, it is not known whether the low frequency electric field noise in Titan's wake region (see Figure 4) is due to electrostatic or electromagnetic waves. Since the Cassini RPWS instrument provides magnetic field measurements, the electrostatic/electromagnetic character of these and other emissions can be determined. The Cassini instrument also has considerably better frequency and time resolution than the Voyager plasma wave instrument. These improvements in the instrumentation, together with the greatly improved spatial coverage provided by the Cassini mission will provide a major advance in our knowledge and understanding of plasma waves in the Saturnian system. With the Cassini RPWS we expect to achieve the following specific results relative to plasma waves in the Saturnian system.

- Establish the spectrum and types of plasma waves associated with gaseous emissions from Titan, the rings, and the icy satellites.
- Determine the role of plasma waves in the interaction of Saturn's magnetospheric plasma (and the solar wind) with the ionosphere of Titan.
- Establish the spectrum and types of plasma waves that exist in the radiation belt of Saturn.
- Determine the wave-particle interactions responsible for the loss of radiation belt particles.
- Establish the spectrum and types of waves that exist in the magnetotail and polar regions of Saturn's magnetosphere.
- Determine if waves driven by field-aligned currents along the auroral field lines play a significant role in the auroral charged particle acceleration.
- Determine the electron density in the magnetosphere of Saturn, near the icy moons, and in the ionosphere of Titan.

2.3. LIGHTNING

Lightning is a fundamental process in Earth's atmosphere and is thought to occur at five other planets: Venus (Ksanfomality *et al.*, 1983; Russell, 1991) (although this is controversial (Gurnett *et al.*, 2001)), Jupiter (Gurnett *et al.*, 1979b; Kurth *et al.*, 1985), Saturn (Warwick *et al.*, 1981; Kaiser *et al.*, 1983; Zarka and Pedersen, 1983), Uranus (Zarka and Pedersen, 1986), and Neptune (Gurnett *et al.*, 1990; Kaiser *et al.*, 1991). A comparison of the characteristics of lightning at these planets is given by Zarka *et al.* (1995). Lightning is usually associated with convective storms, although in rare cases it is also known to be caused by volcanic activity. At Earth, lightning discharges occur when the electric field caused by charge separation in a convective storm exceeds the breakdown field of the atmosphere (Uman, 1987). Because of the high temperatures generated along the discharge path, lightning induces chemical reactions that otherwise would not occur in planetary atmospheres. For example, in Jupiter's atmosphere the dissociation of CH_4, NH_3, H_2S, and H_2O

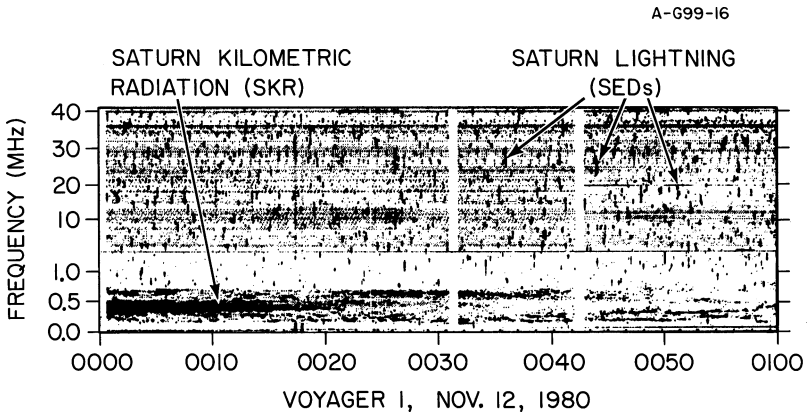

Figure 5. A frequency-time spectrogram of the electric field intensities detected by the planetary radio astronomy (PRA) instrument during the Voyager 1 flyby of Saturn (illustration adapted from Kaiser *et al.*, 1984b). The impulsive bursts scattered randomly around the spectrogram are believed to be due to lightning in Saturn's atmosphere and are called Saturn Electrostatic Discharges (SEDs). A persistent level of Saturn kilometric radiation (SKR) can also be seen near the bottom of the spectrogram, from about 100 to 800 kHz.

is believed to be primarily caused by the high temperatures associated with lightning discharges (Prinn and Owen, 1976). Similar processes are believed to occur in Saturn's atmosphere (Prinn *et al.*, 1984). When organic molecules are present in the atmospheric gas, it has also been demonstrated that electrical discharges can generate complex amino acids that are the building blocks of living organisms (Miller, 1955).

Lightning was first discovered in the atmosphere of Saturn by Voyager 1. During the Voyager 1 flyby, very intense impulsive bursts of radio noise, called Saturn electrostatic discharges (SEDs), were detected by the Planetary Radio Astronomy experiment (Warwick *et al.*, 1981). A frequency-time spectrogram showing a large number of SEDs is shown in Figure 5. At first the origin of these bursts was not clear. However, later analyses by Burns *et al.* (1983) and Kaiser *et al.* (1983) provided strong evidence that the bursts originated from lightning in the equatorial region of Saturn's atmosphere. The rate of occurrence of SEDs showed a persistent periodicity ranging from about 10.0 to 10.16 h, substantially less than the 10.66-h periodicity of the SKR, which as described earlier gives the rotational period of Saturn's deep interior. The shorter period of the SED events is believed to be due to strong prograde equatorial winds that carry convective storms eastward relative to the rotation of Saturn's interior. Typical SED bursts have a duration of 30–400 ms, and involve the radiation of 10^6–10^9 Joules of energy at radio frequencies. The frequency range of these bursts extends from as low as 20 kHz to as high as 40 MHz (Zarka and Pedersen, 1983), and the spectrum has a well-defined low frequency cutoff. The low frequency cutoff varies from about 6 to 15 MHz for storms located on the dayside of Saturn, to less than 300 kHz for storms located on the nightside

of Saturn. The low frequency cutoff is believed to be caused in the ionosphere of Saturn by the well-known cutoff of free-space electromagnetic radiation at the local electron plasma frequency. This cutoff has been used to measure the electron density in Saturn's ionosphere (Kaiser *et al.*, 1984b). Typical peak electron densities vary from about 4×10^5 cm^{-3} on the dayside of Saturn to less than 10^3 on the nightside of Saturn. Under some circumstances absorption is also believed to play a role in the low frequency cutoff of the lightning signal as it passes through the ionosphere (Zarka, 1985a). For a review of SEDs and the effect of the ionosphere on the received lightning spectrum, see Zarka (1985b). Although wideband waveform measurements were obtained at frequencies below about 10 kHz by both the Voyager 1 and 2 plasma wave instruments, no whistlers were detected from lightning, most likely because the spacecraft did not pass through magnetic field lines that connected with the low-latitude lightning source.

One of the outstanding results from the Voyager 1 flyby of Saturn was the discovery of organic molecules in the atmosphere of Titan (Hanel *et al.*, 1981). These organic molecules are believed to be produced primarily by photosynthesis due to solar ultraviolet radiation. However, since lightning could be important for synthesizing complex organic molecules (Sagan and Khare, 1971), a careful search for lightning in Titan's atmosphere was carried out during the Voyager 1 flyby of Titan (Desch and Kaiser, 1990). No evidence of lightning was found. However, because of the poor sensitivity of the Voyager radio instrument at high frequencies, and the lack of complete line-of-sight coverage of the entire atmosphere, it is still believed that weak or very localized lightning discharges could exist in Titan's atmosphere (Lammer *et al.*, 2001).

Because of the long observing time in the vicinity of Saturn, and the numerous close flybys of Titan, the Cassini mission provides an ideal opportunity to improve our knowledge of lightning in the atmosphere of Saturn, and to definitely establish whether lightning exists at Titan. The RPWS instrument is expected to have a sensitivity that is about a factor of one hundred better than Voyager for detecting impulsive lightning-like signals at high frequencies (above the ionospheric cutoff), and a sensitivity comparable to Voyager for detecting whistler-mode waves produced by lightning. In addition the RPWS has the capability of performing direction-finding measurements, a capability that did not exist with Voyager. Direction-finding measurements can be used, for example, to determine the location of lightning storms in the atmosphere of Saturn and to track these storms as they evolve. With the Cassini RPWS we expect to achieve the following specific results relative to lightning.

- Establish the long-term morphology and temporal variability of lightning in the atmosphere of Saturn.
- Determine the spatial and temporal variation of the electron density in Saturn's ionosphere from the low frequency cutoff and absorption of lightning signals.
- Carry out a definitive search for lightning in Titan's atmosphere during the numerous close flybys of Titan.

- Perform high-resolution studies of the waveform and spectrum of lightning in the atmosphere of Saturn, and compare with terrestrial lightning.

2.4. Thermal Plasma

The electron number density and temperature of the thermal plasma are among the most important parameters of a plasma. Together with the magnetic field they control the dispersion and damping of waves and are key quantities in many other plasma processes. Although these parameters are important, they are also difficult to measure, particularly with direct particle detection techniques. In fact, one of the major problems encountered in interpreting the Voyager observations was the uncertainty in the plasma density (Scarf *et al.*, 1984; Neubauer *et al.*, 1984). Two effects contribute to these difficulties. First, photoelectron emission from the spacecraft body produces a local non-thermal plasma that makes it difficult to detect the ambient plasma, particularly at low energies below a few tens of electron volts. Second, charges that accumulate on the spacecraft body produce strong local electric fields that prevent certain classes of particles from reaching the detector (electrons if the spacecraft is charged to a negative potential and ions if the spacecraft is charged to a positive potential). Although these effects can be minimized by various techniques, they are almost always a major concern, particularly when the plasma is hot and tenuous.

Plasma wave measurements of various characteristic plasma resonances provide a powerful and very accurate technique for determining certain basic plasma parameters, such as the electron density and temperature. Since the wavelengths of the waves responsible for the plasma resonances are usually much larger than the dimensions of the spacecraft, the resonance frequencies are usually completely unaffected by the presence of the spacecraft. Probably the most important characteristic resonance frequency of a plasma is the electron plasma frequency, f_{pe}, which as described earlier is directly proportional to the square root of the electron density. The upper hybrid resonance, f_{UHR}, is another very important resonance that can be used to determine the electron density. If the electron cyclotron frequency, f_{ce}, is known from magnetic field measurements, as it usually is, then it is easy to show that the electron density can be determined from the upper hybrid resonance frequency by using the equation, $n_e = [(f_{pe}^2 - f_{ce}^2)/8980]\ \mathrm{cm}^{-3}$, where the frequencies are in Hz.

Two plasma wave techniques can be used to determine the characteristic resonance frequencies of a plasma: passive and active. Passive measurements rely on thermal fluctuations or plasma instabilities to excite the characteristic resonance frequencies in the plasma. A good example of the passive technique is illustrated in Figure 6 , which shows a frequency-time spectrogram of the electric field intensities observed by the Galileo plasma wave instrument during the close flyby of Earth that occurred on December 8, 1992. The narrow line labeled “thermal plasma line” is caused by thermal excitation of electrostatic oscillations at the electron plasma

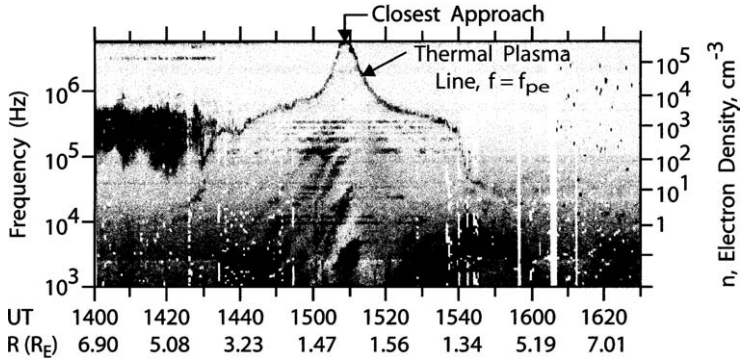

Figure 6. A frequency-time spectrogram of the electric field intensities detected by the Galileo plasma wave instrument during the close flyby of Earth that occurred on December 8, 1992. The narrow emission line labeled "thermal emission" is caused by thermal excitation of electrostatic oscillations at the electron plasma frequency. This emission line can be used to determine the local electron density, which is shown by the scale of the right.

frequency (also called Langmuir waves). Since the electron plasma frequency is directly proportional to the square root of the electron density, the oscillation frequency can be converted directly to electron density. A corresponding electron density scale is shown on the right-hand side of the plot. The sharp peak centered on closest approach is due to the passage through Earth's ionosphere. Although not shown, the electron temperature also can be computed from the spectral shape of the emission line. For a discussion of the techniques used to compute the electron temperature, see Meyer-Vernet and Perche (1989). The main requirement for reliable measurements with the passive technique is that the length of the electric antenna be substantially greater than the Debye length, λ_D, which is given by $\lambda_D = 6.9\sqrt{T_e/n_e}$ cm, where T_e is the electron temperature in °K, and n_e is the electron density in cm^{-3} (Stix, 1992). Otherwise, the thermal plasma line becomes very diffuse and poorly defined. Since the Debye length increases as the electron temperature increases and the density decreases, the technique works best in cold dense plasmas, such as planetary ionospheres. During the Cassini mission the primary application of the passive resonance technique is expected to be the ionosphere of Titan. As the spacecraft passes through the ionosphere of Titan we expect to obtain electric field spectrograms comparable to Figure 6 , from which the electron density can be directly determined to an accuracy of a few percent.

The main disadvantage of the passive resonance technique is that the thermally excited plasma line is very weak, typically only a few dB above the receiver noise level, and becomes very diffuse and difficult to measure when the Debye length is large. Therefore, under some circumstances it is not possible to measure the electron density using passive techniques. For example, in Figure 6 the thermal plasma line becomes very difficult to detect in the hot tenuous magnetospheric plasma before about 1425 UT, and after about 1540 UT. To assure that we can measure the electron density under all circumstances, the RPWS also includes an active method

of exciting plasma resonances. Active excitation of plasma resonances has been performed for many years in Earth's magnetosphere, and is usually called plasma sounding (Lockwood, 1963; Benson, 1970; Etcheto and Bloch, 1978; Harvey *et al.*, 1979; Decreau *et al.*, 1987). Plasma sounding consists of transmitting a short pulse at a fixed frequency, and then "listening" for a resonant response from the plasma. After each pulse the transmitter frequency is increased by a small amount, eventually scanning the entire frequency range of interest. When a resonance is encountered, the received signal is strongly enhanced. The duration of the resonant response depends on a number of factors, including thermal (Landau) damping of the excited wave and convection of the wave packet away from the spacecraft. Resonant effects are typically observed at the electron plasma frequency, f_{pe}, the upper hybrid resonance frequency, f_{UHR}, the harmonics of the electron cyclotron frequency, nf_{ce}, and a series of resonances called the q-resonances, f_q, that occur between the electron cyclotron harmonics. The resonance at the electron plasma frequency can provide very accurate measurements of the electron density, and if the q-resonances are sufficiently separated from the electron cyclotron harmonics these resonances can provide measurements of the electron temperature (Etcheto *et al.*, 1983).

In addition to the plasma wave method of studying the thermal plasma, the RPWS instrument also includes a Langmuir probe for measuring the electron density and temperature. The Langmuir probe technique consists of applying a bias voltage to the probe, a sphere in our case, and measuring the current to the probe as a function of the bias voltage (Mott-Smith and Langmuir, 1926). For a positive bias voltage it can be shown that the current is directly proportional to the electron number density. For negative bias voltages the current depends mainly on the thermal motions of the electrons. Only electrons with enough kinetic energy to overcome the electrostatic potential barrier imposed by the bias voltage contribute to the current. In this negatively biased regime it can be shown that the electron temperature is inversely proportional to the slope of the logarithm of the current plotted as a function of the bias voltage. Thus, the Langmuir probe can also be used to determine the electron temperature, a quantity that is difficult to measure using wave techniques. One problem with the Langmuir probe technique is that spacecraft charging effects cause an offset in the voltage scale relative to the potential in the plasma. However, this offset can be determined from the shape of the current-voltage characteristic of the probe. Photoelectrons also complicate the interpretation of Langmuir probe data. For positive bias voltages of more than a few volts, all of the photoelectrons are attracted back to the probe. Photoelectrons from the probe then have no effect on the current-voltage characteristics of the probe. However, photoelectrons from the spacecraft are now attracted to the probe, and these give a lower limit on the electron number density that can be measured. For a 1 eV plasma at Saturn, this lower limit is about 1 cm^{-3}. Somewhat lower densities are reachable in eclipse conditions. The spacecraft body and its surrounding plasma sheath also affects the current-voltage characteristics of the probe. To avoid

disturbances from the spacecraft body the Debye shielding length, λ_D, should be significantly smaller than the distance from the probe to the spacecraft. For the probe geometry used on Cassini and a plasma temperature of 1 eV, this restriction places a lower limit on the electron densities that can be determined accurately of about 25 cm^{-3}. Lower densities are measurable, but the interpretation will be more difficult. Since the electron densities in the ionosphere of Titan are expected to be much greater than 25 cm^{-3}, the Langmuir probe should be able to provide accurate measurements of the electron density and temperature in the ionosphere of Titan. If the plasma density is sufficiently high, it is also expected that the Langmuir probe can provide useful measurements in the vicinity of the icy moons and in the inner regions of the magnetosphere.

With the RPWS we expect to achieve the following specific results relative to the density and temperature of the thermal plasma.

- Determine the spatial and temporal distribution of the electron density and temperature in Titan's ionosphere.
- Characterize the escape of thermal plasma from Titan's ionosphere in the downstream wake region.
- Constrain and, when possible, measure the electron density and temperature in other regions of Saturn's magnetosphere.

2.5. Dust

The Saturn system is known to contain a large number of very small dust particles, with sizes on the order of a few microns (Smith *et al.*, 1981; Esposito *et al.*, 1984). Imaging measurements with Voyagers 1 and 2 show that the micron-sized particles are heavily concentrated near the ring plane at radial distances near and inside the G ring. These particles are most likely produced by micro-meteoroid impacts on the rings and icy moons. Such very small particles are important for several reasons. First, since they evaporate rapidly, these particles are an important source of magnetospheric plasma. Second, because of their large numbers they also act as a significant absorber of energetic radiation belt particles, thereby contributing to the loss of particles from Saturn's radiation belt. Third, since the dust particles are maintained in a charged state by photoelectron emission, electrostatic and electromagnetic forces can lead to a variety of non-Keplerian effects (Mendis *et al.*, 1984), including acceleration to high energies. Goertz and Morfill (1983) have suggested that the interaction of charged dust particles with the magnetosphere of Saturn could be a significant source of field-aligned currents in the inner regions of Saturn's magnetosphere.

During the Voyager 2 flyby of Saturn, the plasma wave and radio astronomy instruments detected impacts of micron-sized particles on the spacecraft (Scarf *et al.*, 1982; Warwick *et al.*, 1982). The signal detected by these instruments is caused by an impact ionization effect. When a small particle strikes a solid surface at

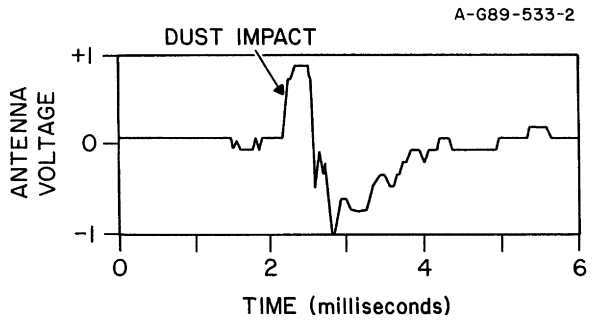

Figure 7. An example of the voltage pulse detected on the Voyager 2 electric field antenna due to a dust impact during the Saturn ring plane crossing on August 26, 1981. These pulses are believed to be due to micron-size particles striking the spacecraft body. Impact rates as high as 600 s^{-1} were observed at the center of the ring plane.

a high velocity (greater than a few km/s), the particle and part of the surface material are vaporized and heated to a very high temperature. The high temperature, $\sim 10^5$ K, causes a substantial amount of the material to be ionized (Hornung and Drapatz, 1981). As the resulting cloud of ionized gas expands over the electric antenna, some of the charge is collected by the antenna, thereby producing a voltage pulse in the receiver. An example of such a voltage pulse is illustrated in Figure 7, which shows the voltage waveform produced by a dust impact during the Voyager 2 ring plane crossing at Saturn (Gurnett *et al.*, 1983). Laboratory measurements show that the charge released is directly proportional to the mass of the particle (Grün, 1981). Since the resulting voltage on the antenna is directly proportional to the charge collected, the pulse amplitude is believed to be directly proportional to the mass of the impacting particle. During the Voyager 2 crossing of Saturn's ring plane, which occurred at 2.88 R_S, the plasma wave instrument detected impact rates as high as several hundred per second. Impact rates of at least 0.1 per second were observed at all radial distances out to at least 35 R_S (Gurnett *et al.*, 1983). Similar dust impact effects were observed by the Voyager 2 plasma wave instrument at Uranus and Neptune (Gurnett *et al.*, 1987, 1991). At sufficiently high impact rates the individual waveforms cause a quasi-continuous spectrum of voltage noise on the antenna, similar to "shot noise" in a vacuum tube. Aubier *et al.* (1983), Meyer-Vernet *et al.* (1986, 1996), Pedersen *et al.* (1991) and others have shown that this shot noise spectrum can be modeled to give information on the number density and mass distribution of the impacting particles. Similar impact ionization effects were also observed and analyzed during the Vega 1 and 2 flybys of Halley (Trotignon *et al.*, 1987; Oberc and Parzydlo, 1992).

With the RPWS we can study the distribution of dust particles in the Saturnian system by using dust impact detection techniques very similar to those used with the Voyager plasma wave and radio astronomy instruments. Several very significant improvements have been made in the RPWS that enhance our ability to detect and analyze dust impacts. On Voyager the waveform measurements were made

by taking the potential difference between the two antenna elements, so that the antenna was operated as a dipole. Because of the dipole response, it was very difficult to estimate the charge released from the impact, and therefore, to estimate the mass of the impacting particle. On Cassini, we plan to directly measure the voltage on the antenna relative to the spacecraft body, similar to the technique that was used by the Voyager radio astronomy investigators. With this system, the charge released by the impact can be determined directly from the amplitude of the voltage pulse on the antenna, thereby giving a signal that is proportional to the mass of the impacting dust particle. On Voyager, the impact waveforms were often saturated because the waveform had only 4-bit resolution. This limitation made it impossible to obtain a meaningful mass estimate from the amplitude of the voltage pulse. The Cassini RPWS uses an automatic gain control and a waveform system with a larger dynamic range (8 bit). With the improved dynamic range it should be possible to routinely obtain mass distributions from pulse height analyses of the observed impact waveforms. An on-board microprocessor algorithm will be used to continuously identify and analyze dust impacts throughout the mission. This method of detecting and analyzing dust particles is expected to complement the measurements from the cosmic dust analyzer (CDA) (see Grün *et al.*, this issue). Although the CDA has a much better capability to analyze the properties of the particles detected, RPWS is expected to be able to detect much lower fluxes since the detecting area for the RPWS is much greater than the aperature area of the CDA. With the RPWS measurements we expect to achieve the following specific results relative to dust impacts.

- Determine the spatial distribution of micron-sized dust particles through out the Saturnian system.
- Measure the mass distribution of the impacting particles from pulse height analyses of the impact waveforms.
- Determine the possible role of charged dust particles as a source of field-aligned currents.

3. Required Instrument Characteristics

To achieve the scientific objectives of the Cassini mission, the instrumentation must have certain design and performance characteristics. This section gives the rationale for the RPWS instrument design and describes the performance required to achieve the scientific objectives described in the previous section. The topics discussed include: (1) field sensors, (2) frequency ranges, (3) frequency and time resolutions, and (4) sensitivities and dynamic ranges.

3.1. Field Sensors

A basic question that arises in the design of all radio and plasma wave instruments is what types of antennas should be used, electric or magnetic, and in each case,

how many field components should be detected. For measurements of radio waves at frequencies well above the local characteristic frequencies of the plasma (i.e., above the electron cyclotron frequency and the electron plasma frequency), the propagation is essentially unaffected by the local plasma. At these frequencies, it is not necessary to measure both the electric and magnetic fields, since they have a constant known ratio, $E = cB$. In principle, it does not matter whether the electric field or the magnetic field is measured. However, for various reasons, both electrical and mechanical, it turns out that an electric antenna can operate at much higher frequencies and with a much greater sensitivity than a magnetic antenna of comparable size and weight (Gurnett, 1998). Therefore, for high frequency radio measurements, such as for SKR and SEDs, an electric dipole antenna is preferred. For plasma waves, which occur at lower frequencies, near or below either the electron cyclotron frequency or the electron plasma frequency, the situation is more complicated. Plasma waves can be either electrostatic, with no magnetic field, or electromagnetic, with both an electric field and a magnetic field. Although an electric antenna can detect both types of waves, the only way to conclusively distinguish an electrostatic wave from an electromagnetic wave is to use both an electric antenna and a magnetic antenna. If a wave can be detected with both an electric antenna and a magnetic antenna, then it is an electromagnetic wave. If it can be detected with an electric antenna, but not with a magnetic antenna, then it is an electrostatic wave. A major shortcoming of the Voyager plasma wave instrument, which used only an electric antenna, was the inability to distinguish electrostatic waves from electromagnetic waves. Therefore, for plasma wave measurements (i.e., at frequencies below either the electron cyclotron frequency or the electron plasma frequency) both electric and magnetic antennas should be used.

Next we consider the number of components to be measured. The Voyager electric field antenna consisted of two cylindrical elements mounted in a V configuration, see Scarf and Gurnett (1977) and Warwick *et al.* (1977). For the plasma wave instrument the two elements were used as a dipole, and for the radio astronomy instrument they were used as two orthogonal monopoles. Although the V configuration provided a limited capability to perform polarization measurements, no capability existed for performing direction-finding measurements. Since the RPWS scientific objectives require accurate determinations of source positions, as well as polarization measurements, it is essential that the RPWS be able to perform both direction finding (i.e., wave normal, $\hat{\mathbf{k}}$) and polarization measurements of high frequency radio signals (i.e., $f > f_{ce}$ and $f > f_{pe}$). Since at high frequencies the electric field is always perpendicular to the wave normal ($\mathbf{E} \cdot \hat{\mathbf{k}} = 0$), the wave normal direction can be determined by measuring the plane of rotation of the electric field (provided the wave is not linearly polarized). Therefore, the RPWS must include full three-axis electric field measurements. The easiest way to achieve this is to use three orthogonal electric monopoles. In the low frequency plasma wave part of the spectrum ($f < f_{pe}$ or $f < f_{ce}$), it is also important to carry out wave normal measurements. Unfortunately, when the anisotropic effects of the plasma

are considered, the wave normal of an electromagnetic wave cannot be determined from electric field measurements. From Poisson's equation, $\nabla \cdot \mathbf{E} = \rho$, one can see that because the charge density, ρ, in a plasma is in general not zero, the electric field is no longer perpendicular to the wave normal, $\mathbf{E} \cdot \hat{\mathbf{k}} \neq \mathbf{0}$. Fortunately, Maxwell's equation $\nabla \cdot \mathbf{B} = \mathbf{0}$ always implies that $\mathbf{B} \cdot \hat{\mathbf{k}} = \mathbf{0}$. Therefore, to make wave normal measurements in the low frequency plasma wave part of the spectral three-axis magnetic field measurements are required. In addition, to assure that electrostatic waves can be detected and to resolve the ambiguity in the direction of propagation (i.e., along $\hat{\mathbf{k}}$ or $-\hat{\mathbf{k}}$), electric field measurements are also required, although these do not necessarily have to be three-axis measurements. In addition to electric field measurements, it is also useful to have the capability to measure electron density fluctuations in the plasma wave frequency range. This capability is easily achieved by biasing the electric antenna element with a known fixed bias current (as though it were a Langmuir probe). With this bias condition, it can be shown that the voltage variations on the element are proportional to the fractional electron density variation, $\delta n_e / n_e$. For electrostatic waves simultaneous measurements of both the electric field and the electron density variation can provide information on the wavelength of the wave (Kelley and Mozer, 1972; Wahlund *et al.*, 1998).

3.2. Frequency Ranges

To decide on the frequency ranges required for the electric and magnetic field measurements, we must consider the characteristic frequencies of the radio and plasma wave phenomena to be studied in the vicinity of Saturn. The frequency ranges and spectrums of all radio and plasma wave phenomena known or predicted to occur in the vicinity of Saturn are summarized in Figures 8–10. Figure 8 shows a model of the electron plasma frequency, f_{pe}, and electron cyclotron frequency, f_{ce}, as a function of radial distance near the equatorial plane on the dayside of Saturn; and Figures 9 and 10 show representative electric and magnetic field spectrums at a radial distance of 10 R_S. First, we consider the upper limit of the frequency range. Two high frequency limits must be considered, one for the electric field and the other for the magnetic field. The high frequency limit for the electric field is determined by the highest radio emission frequency of interest, and the high frequency limit for the magnetic field is determined by the highest plasma wave frequency of interest. As can be seen in Figure 8, lightning from Saturn's atmosphere (SEDs) has the highest frequencies. From the Voyager observations it is known that the SED spectrum extends up to at least 40 MHz. Since the shape of the high frequency part of the SED spectrum is already known (Zarka and Pedersen, 1983), we do not plan to make electric field measurements as high as 40 MHz. Our primary objectives relative to SEDs are to monitor the long-term occurrence of lightning and to study variations in the low frequency cutoff imposed by Saturn's ionosphere. For these purposes it is only necessary to measure the SED spectrum to frequencies slightly greater than the maximum ionospheric cutoff frequency. Since the maximum plasma frequency

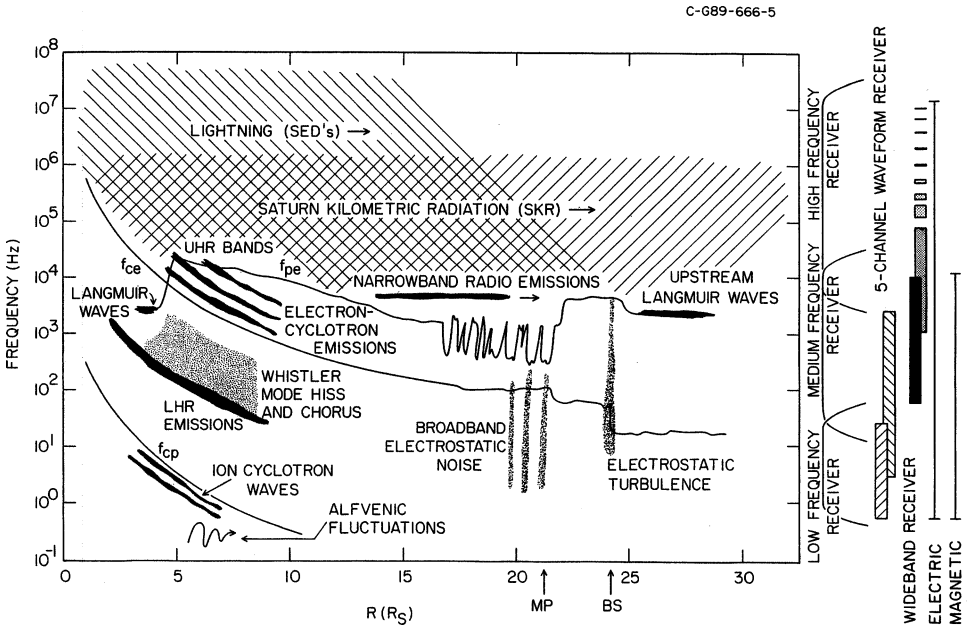

Figure 8. A summary of all the radio and plasma wave phenomena known and predicted to occur in the vicinity of Saturn displayed as a function of frequency and radial distance from Saturn. The bow shock (BS) and magnetopause (MP) positions, indicated by the arrows at the bottom of the plot, are representative of the dayside subsolar region.

of the dayside ionosphere is typically about 5 MHz, we have selected 16 MHz as the upper frequency limit for the electric field measurements. Since the ionospheric cutoff frequency varies as $f_{\text{cutoff}} = f_{\text{pe}}/\cos\theta$, where θ is the angle of incidence, this upper frequency limit allows the detection of lightning over a large range of incidence angles, approximately $0 \leq \theta \leq 70^{\circ}$.

For the upper frequency limit of the magnetic field measurements we must consider the highest plasma wave frequency that is likely to be encountered in Saturn's magnetosphere. As discussed earlier, magnetic field measurements have two main purposes: (1) to distinguish electrostatic waves from electromagnetic waves, and (2) to determine the wave normal direction of electromagnetic waves. During the baseline tour, the periapsis radial distance is expected to be in the range from about 4 to 6 R_S, and the apoapsis is in the range from about 20 to 130 R_S. As can be seen from Figure 8 , the whistler mode, which is the highest frequency electromagnetic plasma wave mode that is likely to be of interest, is generally in the range from 3 to 10 kHz, with a maximum of about 12 kHz. Based on this magnetic field model we have selected 12 kHz as the upper limit for the magnetic field measurements. This allows magnetic field measurements with a simple tri-axial search coil magnetometer, which can be easily designed to respond to frequencies up to 12 kHz. In selecting this upper limit we realize that it will not be possible to

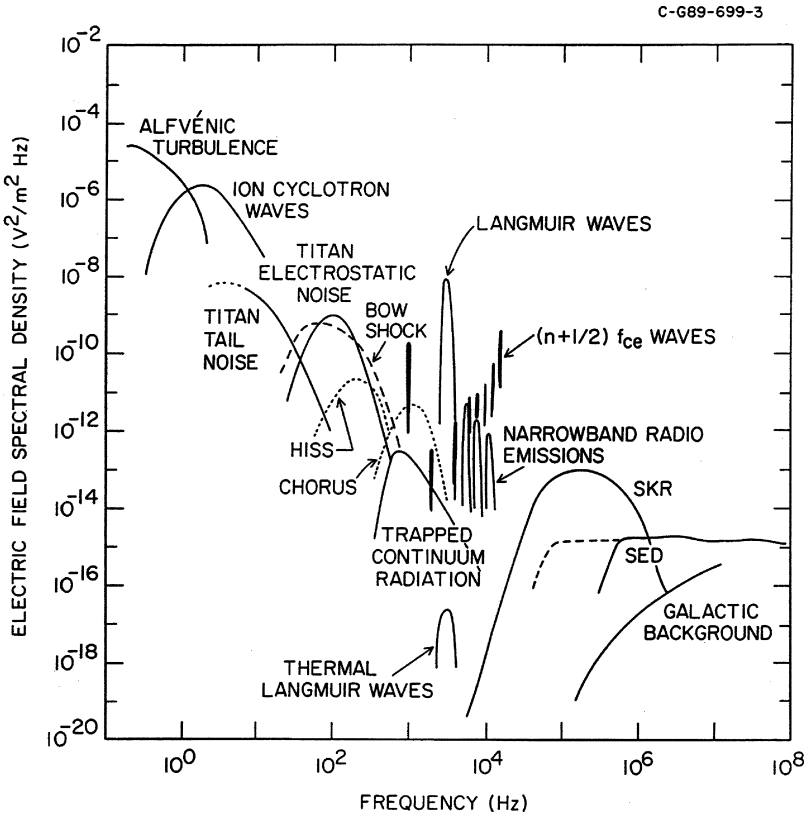

Figure 9. Typical electric field spectral densities of various radio emissions and plasma waves that are known to occur in the magnetosphere of Saturn. To a first approximation the SKR and SED intensities vary inversely as the square of the radial distance from Saturn, and are shown at a representative radial distance of 10 R_S.

detect the magnetic field of certain plasma wave modes that occur at frequencies above 12 kHz. For example, during the Titan flybys UHR emissions are expected to extend up to frequencies as high as several hundred kHz, and during Saturn orbit insertion (SOI), which is at about 1.3 R_S, electrostatic $(n+1/2)\,f_c$ electron cyclotron waves could extend up to frequencies as high as several hundred kHz. However, in all of these cases we feel confident that it will be easy to identify these electrostatic modes. For example, at Titan the UHR emissions will be at frequencies of ten to several hundred kHz, well above the electron cyclotron frequency, which is the highest frequency for the whistler mode. The situation is more complicated near SOI, where whistler-mode emissions could occur at frequencies as high as 500 kHz. To provide magnetic field measurements at such high frequencies would require the use of a loop antenna (Gurnett, 1998). Although such antennas have been flown in the past, they are large and very difficult to accommodate on the spacecraft, so a decision was made that high frequency magnetic field measurements were not

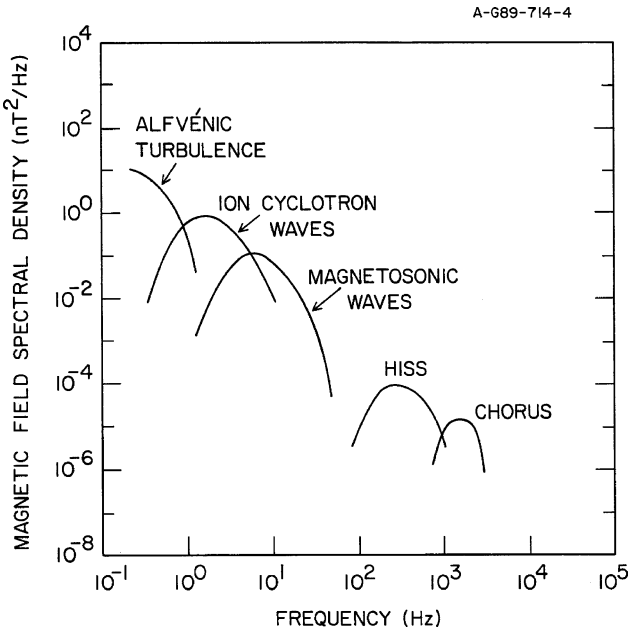

Figure 10. Typical magnetic field spectral densities of various radio emissions and plasma waves that are known to occur in the magnetosphere of Saturn.

justified to achieve this limited objective, given the additional resources that would be required.

Next, we consider the low frequency limit of the plasma wave spectrum. Since scientifically interesting plasma wave phenomena exist down to essentially zero frequency, the low frequency cutoff of the RPWS electric and magnetic field sensors is determined almost entirely by technical considerations. For example, conventional static field magnetometers tend to have better sensitivities than search coil magnetometers at frequencies below about 1 Hz. Since a tri-axial static field magnetometer (MAG) is included on Cassini (Southwood *et al.*, this issue), there is no reason to extend the frequency range of the RPWS magnetic antenna below about 1 Hz. Therefore, we have adopted 1 Hz as the low frequency cutoff of the RPWS magnetic field measurements. For the electric field antennas the situation is more complicated. The frequency response of the electronics for the electric field measurements could easily be extended below 1 Hz. However, because of sheath effects around the spacecraft body, such low frequency, quasi-static, electric field measurements require very long antennas, typically with lengths at least ten times the maximum dimension of the spacecraft body. Since such long antennas ($\sim$100 m, tip-to-tip) could not be accommodated on Cassini due to spacecraft dynamics considerations, we have arbitrarily defined the low frequency cutoff of the RPWS electric field measurements to be the same as for the magnetic field measurements (i.e., 1 Hz).

3.3. Frequency and Time Resolutions

It is well known that the frequency and temporal structure of Saturnian radio emissions and plasma waves vary over an extremely large range (Scarf *et al.*, 1984; Zarka, 1998). Some types of waves, such as continuum radiation and whistler-mode hiss, have smooth continuous spectrums that can be resolved with very modest frequency and time resolution. On the other hand, certain other types of waves, such as lightning-generated whistlers, whistler-mode chorus, and cyclotron maser radiation, have extremely complicated frequency-time structures. These structures often extend down to frequency and time resolutions on the order of $\Delta f \Delta t \sim 1$. Furthermore, in some cases it is necessary to stress high frequency resolution (i.e., small Δf), such as in the analysis of plasma resonances, whereas in other cases it is necessary to stress high-time resolution (i.e., small Δt), such as in the analysis of lightning and dust impacts. Resolving these conflicting demands is one of the main challenges that must be faced in designing a radio and plasma wave investigation.

What little is known about the fine structure of radio emissions and plasma waves at Saturn comes almost entirely from the Voyager measurements. The Voyager plasma wave instrument had a 16-channel spectrum analyzer spanning the frequency range from 10 Hz to 56 kHz, and a wideband waveform receiver that covered the frequency range from 50 Hz to 10 kHz. The time resolution of the 16-channel measurements was 4 s. During selected intervals, the wideband waveform provided high-resolution 48-s "snapshots" of the electric field waveform with a sample rate of 28,800 samples/s. However, the number of wideband frames that could be transmitted was severely limited by data rate considerations. The Voyager planetary radio astronomy instrument, which made measurements from 20 kHz to 40 MHz, had somewhat better frequency resolution ($\Delta f/f \sim$ 1–5%), but relatively poor time resolution ($\sim$6 s/sweep). Although the radio astronomy instrument also included a high-rate mode that allowed rapid (millisecond) sampling of a selected channel, again the amount of high-rate data collected was severely limited.

Since it is highly likely that radio emissions and plasma waves in Saturn's magnetosphere have fine-scale structures comparable to those observed in the Earth's magnetosphere, it is important that the RPWS instrument be designed with sufficient frequency and time resolution to resolve these structures. In particular, the RPWS should provide a substantial improvement relative to the Voyager radio and plasma wave instruments. Our basic approach to achieving this goal is to make measurements on two widely different frequency and time scales: nearly continuous low-rate spectral measurements with a frequency resolution on the order of a few percent and a time resolution on the order of a few seconds, and short-duration high-rate wideband waveform measurements with frequency and time resolutions approaching the limit, $\Delta f \Delta t \sim 1$. The low-rate survey measurements will allow us to produce frequency-time spectrograms comparable to Figure 6 (from the Galileo plasma wave instrument). To provide flexibility, the frequency and time resolution of the low-rate measurements must be controlled by a reprogrammable microprocessor, so that

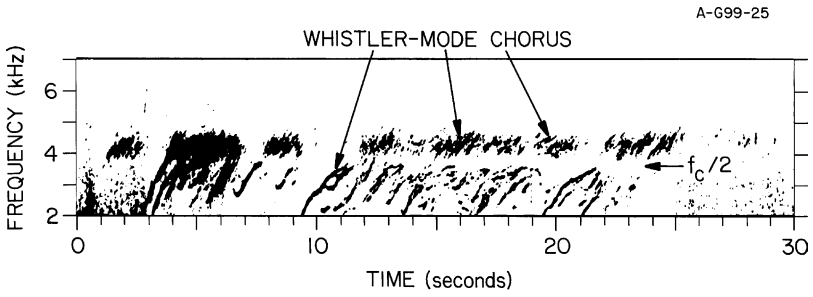

Figure 11. A high-resolution frequency-time spectrogram of whistler-mode chorus observed in Earth's magnetosphere. These emissions are produced by a cyclotron resonance interactions with energetic radiation belt electrons. The fine structure is caused by nonlinear resonant particle trapping effects. Note the prominent gap at one-half the electron cyclotron frequency, $f_c/2$.

they can be changed to accommodate unexpected results. The high-rate wideband waveform measurements will allow us to produce frequency-time spectrograms comparable to Figure 11, which shows a spectrogram of whistler-mode chorus in Earth's magnetosphere. Since the entire waveform is transmitted to the ground, these measurements have the advantage that the frequency and time resolution of the spectral processing can be adjusted during the ground processing to provide the optimum resolution for the phenomena being investigated, the only limit being that $\Delta f\,\Delta t \gtrsim 1$. To provide high-resolution measurements of high frequency radio emissions, the waveform receiver must also have a frequency conversion mode of operation that can provide waveform measurements in selected frequency bands at high frequencies. This mode of operation will allow us to determine whether SKR has fine structure comparable to terrestrial AKR. A frequency-time spectrogram showing the fine structure of terrestrial AKR using this type of frequency conversion mode of operation is shown in Figure 12. As can be seen, terrestrial AKR has fine structure extending down to bandwidths of only a few hundred Hz and time scales of tens of milliseconds, or less. Such high-resolution measurements of SKR will provide fundamental constraints on the mechanism by which these radio emissions are generated.

3.4. Sensitivities and Dynamic Ranges

The RPWS instrument must have sufficient sensitivity to detect the weakest signals of interest in the vicinity of Saturn, and still have adequate dynamic range to respond to the strongest signals without saturating. Figures 9 and 10 show the range of electric and magnetic field strengths that must be measured for various phenomena in the vicinity of Saturn. For some phenomena, such as the SKR and SED events, the intensities vary considerably. In these cases, the spectrums were selected from periods of relatively high intensity at a radial distance of 10 R_S. As

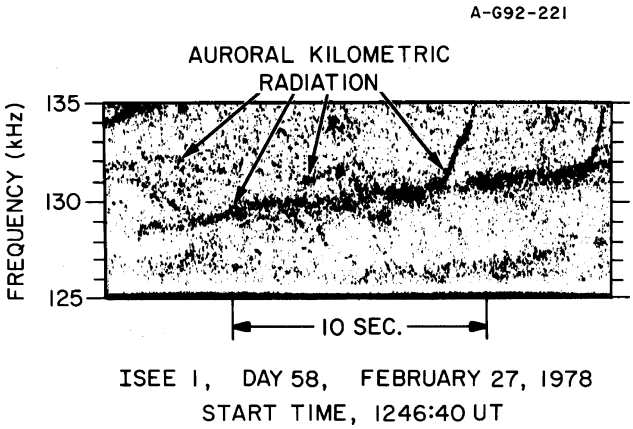

Figure 12. A high-resolution frequency-time spectrogram of terrestrial auroral kilometric radiation (AKR) showing the extremely complicated fine structure of this radiation. The fine structure is most likely caused by nonlinear resonant particle trapping effects, similar to chorus. The Cassini RPWS should be able to determine whether SKR has similar fine structure.

can be seen, the intensities vary over a wide range. For electric fields the spectral densities that must be measured range from a minimum of about 10^{-18} V^2 m^{-2} Hz^{-1} at 10^6 Hz, to a maximum of about 10^{-6} $V^2m^{-2}Hz^{-1}$ at 1 Hz, a total range of 120 dB. For the magnetic field the spectral densities that must be measured range from a minimum of about 10^{-7} nT^2 Hz^{-1} at 10^3 Hz to a maximum of about 10^1 nT^2 Hz^{-1} at 1 Hz, a total range of 80 dB. Since it is very difficult to achieve a total dynamic range of 120 dB, special techniques must be used to accommodate this very large range of signal strengths. For example, since the intensities tend to increase toward lower frequencies, the gain near the front end of the receiving system must be decreased at low frequencies in order to avoid saturation when strong low frequency signals are present. Also, since digital waveforms typically cannot accommodate such large dynamic ranges, automatic gain control systems must be used for all waveform measurements. These and a variety of other techniques must be used in order to assure that the instrument can perform reliable measurements over the large range of field strengths illustrated in Figures 9 and 10 .

4. Instrument Description

The RPWS instrumentation consists of three electric antennas, three magnetic antennas, a Langmuir probe and its associated electronics, and five specialized receivers designed to address the scientific objectives and performance requirements discussed in the two previous sections. In this section we describe each of these elements of the instrument.

4.1. Block Diagram

A simplified block diagram of the RPWS instrument is shown in Figure 13. Three monopole electric field antennas, labeled E_u, E_v, and E_w, are used to provide electric field signals to the various receivers. The orientations of these three antennas relative to the x, y, and z axes of the spacecraft are shown in Figure 14. By electronically taking the difference between the voltages on the E_u and E_v monopoles, these two antennas can be used as a dipole, E_x, aligned along the x-axis of the spacecraft. The E_u and E_v antennas also can be used to sound the local plasma by transmitting short pulses. In an alternate mode of operation, they can be biased and used as Langmuir probes to measure the phase velocity of density structures in the plasma. The tri-axial search coil magnetic antennas, labeled B_x, B_y, and B_z in Figure 13, are used to detect three orthogonal magnetic components of electromagnetic waves. The search coil axes are aligned along the x, y, and z axes of the spacecraft. The spherical Langmuir probe, shown at the bottom of the block diagram, is used for electron density and temperature measurements. Both the electric antennas and the Langmuir probe can be used to detect dust impacts.

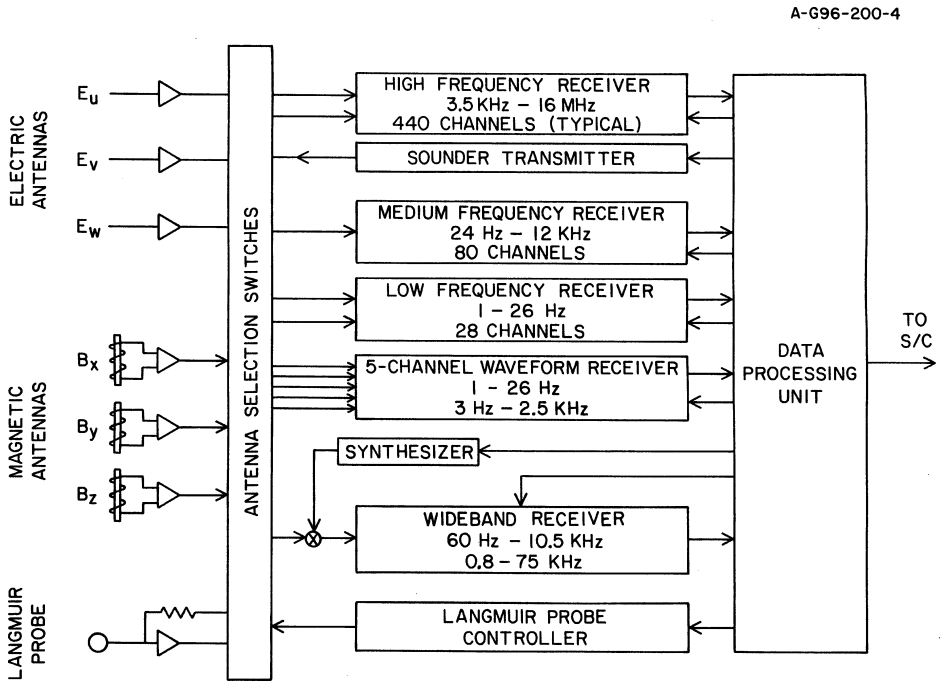

Figure 13. A functional block diagram of the RPWS instrument. The seven sensors, three electric, three magnetic, and the Langmuir probe are shown on the left side. In the middle, the several receivers which the instrument uses to analyze the signals are shown. The data management and control functions, as well as the interface with the spacecraft are shown as the data processing unit on the right side.

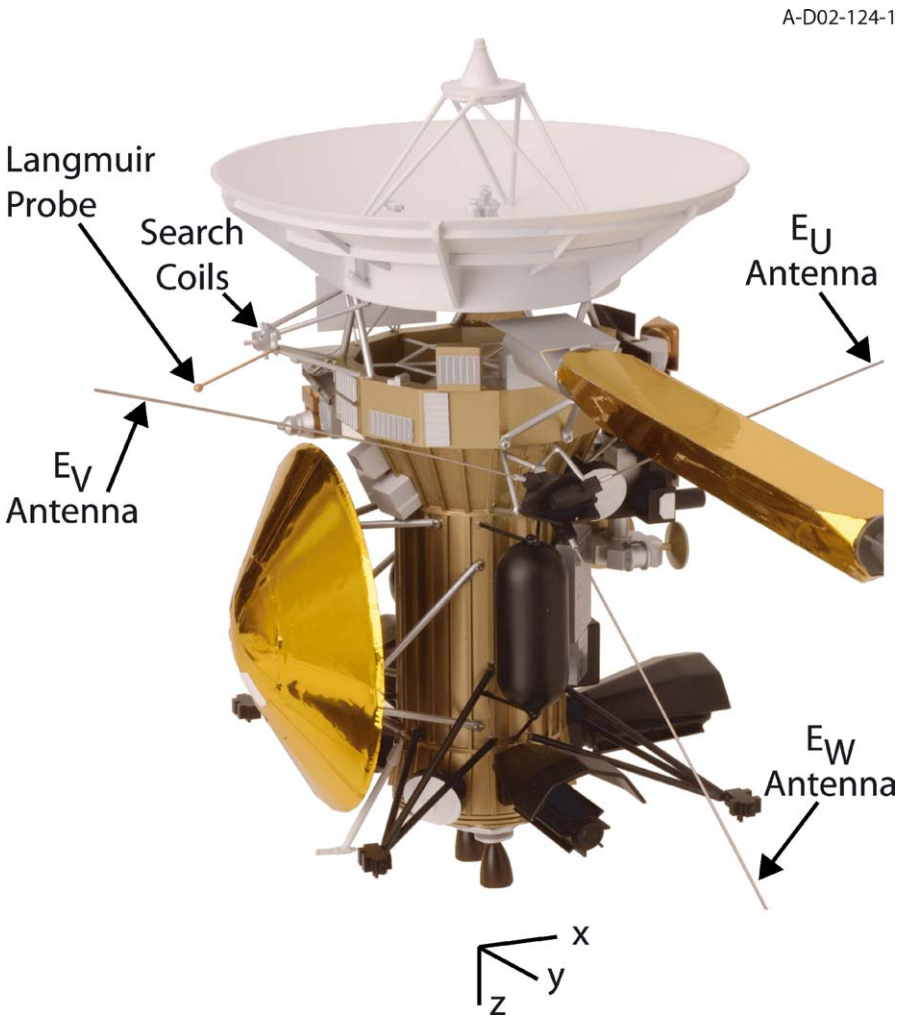

Figure 14. The Cassini spacecraft showing the locations of the RPWS sensors and their relationship with other structures on the spacecraft.

Next, we consider the function of the five receivers shown in the middle column of the block diagram in Figure 13 . These receivers are connected to the antennas described above by a network of switches in the block labeled “antenna selection switches,” the details of which are not shown. The high frequency receiver (HFR) provides simultaneous auto- and cross-correlation measurements from two selected antennas over a frequency range from 3.5 kHz and 16 MHz. By switching the two inputs of this receiver between the three monopole electric antennas, this receiver can provide direction-of-arrival measurements, plus a full determination of the four Stokes parameters. The high frequency receiver includes a processor that performs all of its digital signal processing, including data compression. The high frequency

receiver also includes a sounder transmitter that can be used to transmit short square wave pulses from 3.6 to 115.2 kHz. When used in conjunction with the high frequency receiver, the sounder can stimulate resonances in the plasma, most notably at the electron plasma frequency, thereby providing a direct measurement of the electron number density. The medium frequency receiver (MFR) provides intensity measurements from a single selected antenna over a frequency range from 24 Hz to 12 kHz. This receiver is usually operated in a mode that toggles every 32 s between the E_x electric dipole antenna and the B_x magnetic search coil, thereby providing spectral information for both the electric and magnetic components of plasma waves. The low frequency receiver (LFR) provides intensity measurements from 1 to 26 Hz, typically from the E_x electric dipole antenna and the B_x magnetic antenna. The five-channel waveform receiver (WFR) collects simultaneous waveforms from up to five sensors for short intervals in one of two frequency bands, either 1 to 26 Hz, or 3 Hz to 2.5 kHz. When connected to two electric and three magnetic antennas, this receiver provides wave normal measurements of electromagnetic plasma waves. The wideband receiver is designed to provide nearly continuous wideband waveform measurements over a bandwidth of either 60 Hz to 10.5 kHz, or 800 Hz to 75 kHz. These waveforms can be analyzed on the ground in either the temporal domain, or in the frequency domain (Fourier transformed) to provide high-resolution frequency-time spectrograms. In a special frequency-conversion mode of operation, the high frequency receiver can provide waveforms to the wideband receiver in a 25-kHz bandwidth that is tuneable to any frequency between 125 kHz and 16 MHz. Table II summarizes the characteristics of the five basic receivers described above.

The Langmuir probe controller shown in the block diagram is used to sweep the bias voltage of the probe over a range from –32 to +32 V in order to obtain the current-voltage characteristics of the probe, and thereby the electron density and temperature. The controller can also set the bias voltage on the E_u and E_v monopoles over a range from –10 to +10 V in order to operate them in a current collection mode for $\delta n_e/n_e$ measurements.

The RPWS data processing unit shown on the right-hand side of the block diagram consists of three processors. The first processor, called the low-rate processor, controls all instrument functions, collects data from the high frequency receiver, the medium frequency receiver, the low frequency receiver, and the Langmuir probe, and carries out all communications with the spacecraft command and data system (CDS). The second processor, called the high-rate processor, handles data from the wideband and five-channel waveform receivers and passes the data along to the low-rate processor for transmission to the CDS. The third processor, called the data compression processor, is primarily used for data compression, but can also perform specialized operations such as on-board dust detection by using waveforms from the wideband receiver.

As shown in Figure 14, the RPWS hardware is mounted in several locations around the Cassini spacecraft. The main electronics package, which includes the

TABLE II
Summary of RPWS receiver characteristics.

Receiver section	Measurements	Spectral range	Spectral resolution	Temporal resolution
High frequency receiver (HFR)	$E_1 = E_u$, E_v or E_x $E_2 = E_w$; $\|E_1\|^2$, $\|E_2\|^2$, Re($E_1 \bullet E_2{}^*$), Im($E_1 \bullet E_2{}^*$)	3.5–318 kHz 0.125–16.125 MHz	$\Delta f/f = 5$, 10, 20% (log); $\Delta f = 3.1$ kHz to $n \times 25$ kHz (linear)	0.1–10 s/spectrum
Medium frequency receiver (MFR)	One of: E_x, E_u, E_v, E_w, B_x, B_z	24–180 Hz; 180 Hz–1.5 kHz; 1.5–12 kHz	$\Delta f/f \simeq 13\%$; $\Delta f/f \simeq 7\%$; $\Delta f/f \simeq 7\%$	16 s/spectrum; 16 s/spectrum; 8 s/spectrum
Five-channel waveform receiver (WFR)	Five of: E_x, E_u, E_v, E_w, B_x, B_y, B_z, LP	~1–26 Hz; 3 Hz–2.5 kHz	0.2 Hz, typical; 3.5 Hz typical	1 data set/5 min, typical, 1 data set/16 s, max
Low frequency receiver (LFR)	Two of: E_x, E_u, E_v, E_w, B_x, B_y, B_z, LP	~1 - 26 Hz	$\Delta f/f = 12\%$	$1E + 1B$ spectrum/16s, typical
Wideband receiver (WBR)	One of: E_x, E_u, E_v, E_w, B_x, LP	60 Hz–10.5 kHz; 0.8–75 kHz	13.6 Hz, typical; 109 Hz, typical	125ms/spectrum, typical

medium frequency receiver and the digital processing unit, resides in bay 4 of the main spacecraft bus. The electric antenna deployment mechanisms and the high frequency receiver are mounted on a bracket on the $+y$ side of the spacecraft, just below the base of the magnetometer boom. The magnetic search coil assembly is supported by a short boom that is attached to the high gain antenna support structure on the $-x$ side of the spacecraft. The Langmuir probe is mounted on the end of an 0.8-m hinged boom that extends outward from the magnetic search coil assembly.

4.2. Electric Antennas

The three electric monopole antennas and their deployment mechanisms were provided by Orbital Sciences Corporation. The antenna elements consist of conducting cylinders, each 10 m long and 2.86 cm in diameter. The elements are made of beryllium-copper, silver plated on the exterior surface, and painted black on the interior for thermal control. Approximately 12% of the surface area is perforated with small holes to allow sunlight to heat the shaded side of the element in order to reduce thermal bending. The elements themselves are formed by two opposing semi-cylindrical strips with interlocking tabs. For launch, the elements are flattened

Figure 15. A photograph of the RPWS electric antenna assembly. The three electric monopole deployment mechanisms are most obvious in this view, however, both the motor control electronics and the high frequency receiver are also part of this assembly.

and rolled onto a spool. During deployment after launch, a motor-driven deployment mechanism feeds the element through a forming channel that expands the strips into a cylindrical tube. A photograph of the three electric antenna deployers, the high frequency receiver, and the associated mounting bracket is shown in Figure 15.

TABLE III
Comparison of physical and electrical orientations of the electric antennas.

	Physical orientation*		Electrical orientation (Rheometry)	
Antenna†	θ (deg)	ϕ (deg)	θ (deg)	ϕ (deg)
E_u	107.5	24.8	107.9	16.5
E_v	107.5	155.2	107.3	162.7
E_w	37	90	31.4	91.2

*The angle θ is the polar angle measured with respect to the spacecraft $+z$ axis, ($\cos\theta = z/\sqrt{x^2+y^2+z^2}$), (and the angle ϕ is azimuth angle measured with respect to the $+x$ axis ($\tan\phi = x/y$).

†In some previous papers (Ladreiter *et al.*, 1995; Rucker *et al.*, 1996) and various engineering documents, E_u, E_v, and E_w antennas are labeled E_{x+}, E_{x-}, and E_z. The u, v, w, notations are used in this paper to avoid confusion with the spacecraft x, y, and z axes.

The physical orientations of the three elements with respect to the x, y, and z axes of the spacecraft are provided in Table III. The E_u and E_v elements are extended symmetrically at angles of 60° with respect to the spacecraft y-z plane. The plane containing these two elements is rotated 37° with respect to the spacecraft x-y plane. These two elements can be used to provide a dipole antenna (E_x) with a tip-to-tip length of 18.52 m parallel to the spacecraft x-axis. The E_w antenna is extended perpendicular to the plane formed by the E_u and E_v elements (i.e., at an angle of 37° from the spacecraft z-axis). Several considerations led to this antenna configuration. First, the three monopoles provide the nearly orthogonal tri-axial configuration required for direction finding. Second, as previously described, the E_u and E_v elements can be operated as a dipole (E_x,), which minimizes common-mode coupling in order to provide the lowest possible level of spacecraft-generated interference. The E_u and E_v elements are also symmetric with respect to the magnetometer boom, which minimizes the effect this boom has on the dipole antenna pattern. Third, the w-axis element is rotated somewhat away from the spacecraft in order to reduce electrical coupling and interference from electrical equipment in the lower bay of the spacecraft. Fourth, the E_u and E_v elements are rotated away from the spacecraft x-y plane so that they do not interfere with the field of view of the stellar reference unit. This orientation also provides clearance for release of the Huygens probe.

The three electric antennas were deployed to their full 10-m length during a 30-h activity on October 25, 1997, ten days after launch. Full deployment was confirmed by both a potentiometer reading and a limit switch indication, the latter being the most reliable indication of full deployment. A brief set of measurements performed subsequent to the deployments verified that each antenna was properly connected to the instrument and that there were no shorts to the spacecraft structure. There are

no plans to retract or otherwise change the length of the elements for the duration of the mission.

Due to the complex shape of the Cassini spacecraft, the effective electrical axes of the monopole antennas differ significantly from their physical orientations. Electrical measurements using a 1:30 scale model of the spacecraft in a tank of electrolytic fluid (rheometry) were performed by Rucker *et al.* (1996). These measurements show angular offsets of the electrical axes by as much as 5 to 6 degrees for the E_{w} antenna, and 7 to 8 degrees for the E_u and E_v antennas (see Table III). Ladreiter *et al.* (1995) have developed an analysis technique that can be used to perform in-flight determinations of the electrical axes by using a point source with known polarization characteristics. Jupiter provides the best source for this purpose and in-flight calibrations of the electrical axes of the antennas were carried out during the Jupiter flyby, which took place in December 2000 and January 2001. Preliminary results of this calibration are given by Vogl *et al.* (2001). Although this calibration occurred with the Huygens probe attached to the spacecraft, the rheometry results show that the electrical axes shift by only a small amount (less than one degree) when the probe is released.

4.3. Magnetic Antennas

The tri-axial search coil magnetic antennas were provided by CETP in Velizy, France. These antennas are mounted on a short, fixed boom just under the high gain antenna on the $-x$ side of the spacecraft, as shown in Figure 14 . The three axes of the search coils are aligned with the x, y, and z axes of the spacecraft. Each search coil utilizes 10,000 turns of 0.07 mm wire wound around a μ-metal core 25 cm long with a cross-sectional area of 15 mm^2. The sensors have a usable frequency range of 1 Hz to 20 kHz. A flux feedback winding is used in each search coil to flatten the frequency response over the range from 30 Hz to 18 kHz. The transfer function in this frequency range is approximately 150 mV/nT. Preamplifiers are mounted at the base of the mounting boom. When the spacecraft $-z$ axis is pointed toward the Sun, as it is whenever the spacecraft is in the inner solar system, the high gain antenna acts as a sun shade for the search coils. Two radioisotope heating units are used to provide an internal heat source for thermal control. A thermal blanket system surrounds the assembly to minimize the radiated heat loss. A photograph of the search coil magnetic antenna assembly is shown in Figure 16.

4.4. Langmuir Probe

The Langmuir probe consists of a 5-cm diameter titanium sphere mounted on the end of a 0.8-m hinged boom that folds outward from one leg of the boom that holds the search coil magnetic antenna assembly. A preamplifier is mounted near the base of the search coil boom. To minimize the influence of photoelectrons,

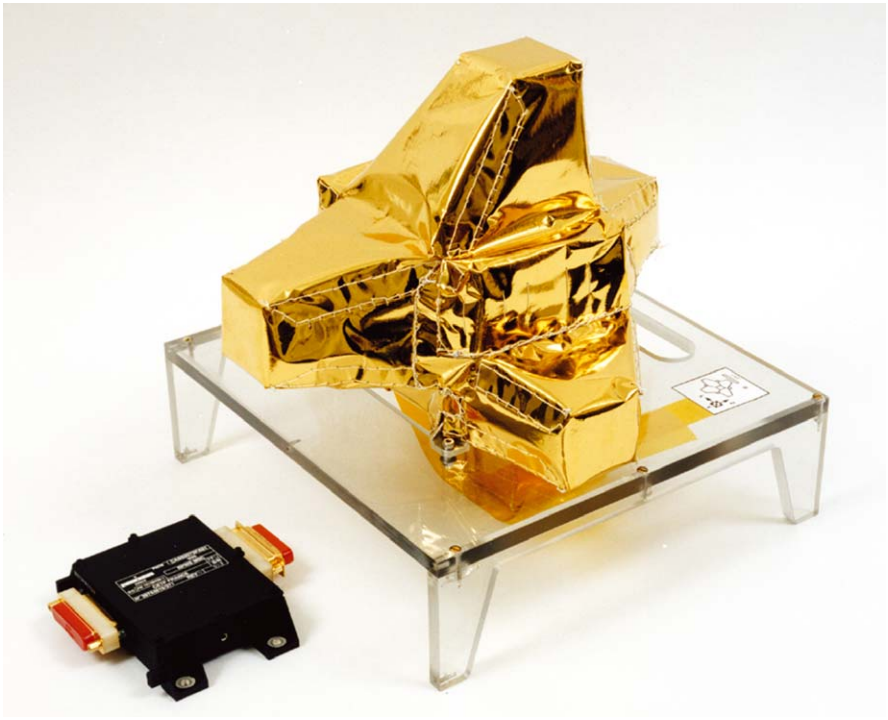

Figure 16. A photograph of the tri-axial magnetic search coil assembly. Thermal blankets are shown as flown.

the outermost 10.9-cm segment of the boom is made as thin as possible (diameter = 6.35 mm) and has an outer guard shield that is held at the same voltage as the probe sphere. In its deployed configuration, the probe is approximately 1.5 m from the nearest spacecraft surface. When the $-z$-axis of the spacecraft is sun-pointed, as it is in the inner solar system, the probe is in the sunlight. The surface of the probe is coated with titanium nitride by baking at high temperature in a nitrogen atmosphere (Whalström *et al.*, 1992). This treatment provides a durable surface with a constant work function so that the potential of the probe surface is uniform. (If the potential varies over the surface, the current-voltage characteristic is adversely affected.) This coating effectively eliminates hysteresis effects, which can occur for other surface coatings. A photograph of the Langmuir probe is shown in Figure 17.

The boom holding the Langmuir probe was deployed on 15 October 1997 as part of the launch sequence. Deployment was verified by noting that the probe emitted the expected photoelectron current when biased to a negative voltage (the spacecraft orientation was such that the probe was in sunlight when deployed).

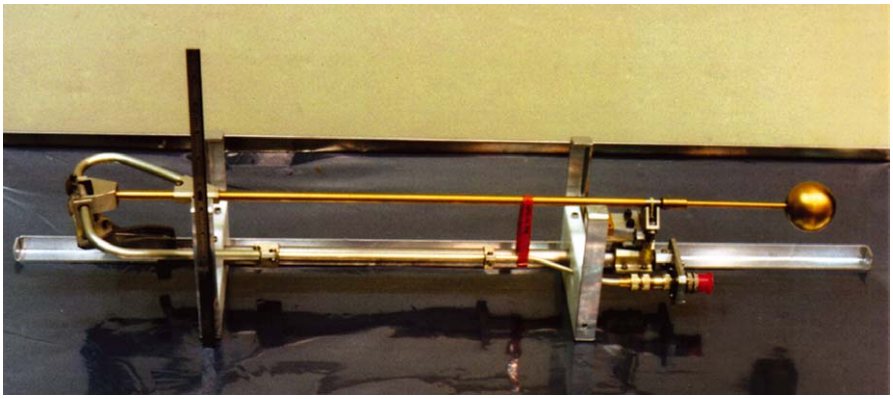

Figure 17. A photograph of the Langmuir probe and boom assembly in its stowed configuration on one of the struts of the tripod that also supports the magnetic search coil assembly.

As mentioned earlier, two of the electric antennas (E_u, E_v) can also be operated as Langmuir probes in a current-collecting mode. This mode is used primarily for studying plasma density variations associated with waves and turbulence. The current measurement range is 1 nA to 100 μA for positive bias voltages, and 100 pA to 100 μA for negative bias voltages.

4.5. High Frequency Receiver

The high frequency receiver consists of two sets of four analog receivers followed by a digital signal processing unit. The design is based on a similar receiver flown on the Wind spacecraft (Bougeret *et al.*, 1995). One set of receivers is connected to the E_w monopole. The other set of receivers can be connected either to the E_x dipole or toggled between the E_u and E_v monopoles. Three of the four receivers have fixed-frequency filters (A, B, and C) that together cover a frequency range from 3.5 to 319 kHz. Each filter covers 2.2 octaves in frequency (i.e., a factor of 4.5). Digital spectral analysis is performed within each of the three filter bands to provide 8, 16, or 32 logarithmically spaced frequency channels, yielding spectral resolutions of 20, 10, or 5%, respectively. The fourth (HF) receiver is tunable over a frequency range from 100 kHz to 16.1 MHz and has a bandwidth of 25 kHz. This receiver can be tuned in two different modes, HF1 and HF2. HF1 provides measurements over a frequency range from 100 kHz to 4.125 MHz in 25-kHz steps. HF2 provides measurements over a frequency range from 125 kHz to 16.125 MHz in 50-kHz steps. Within the 25 kHz passbands of HF1 or HF2, it is possible to have either 1, 2, 4, or 8 linearly spaced channels, thereby giving frequency resolutions of 25, 12.5, 6.25, and 3.125 kHz. The high frequency receiver has an automatic

TABLE IV
Characteristics of the high frequency receiver.

Band	Frequency range	Frequency steps	Frequency resolution	Integration times
A	3.5–16 kHz	8, 16, or 32 (logarithmic)	20, 10, or 5%	0.125, 0.25, 0.5, or 1 s
B	16–71 kHz	8, 16, or 32 (logarithmic)	20, 10, or 5%	0.125, 0.25, 0.5, or 1 s
C	71–319 kHz	8, 16, or 32 (logarithmic)	20, 10, or 5%	0.125, 0.25, 0.5, or 1 s
HF1	125 kHz–4.125 MHz	n × 25 kHz; 1, 2, 4, or 8 linear channels within 25-kHz band	3.125, 6.25, 12.5, 25, or n × 25 kHz	20, 40, 80, or 160 ms
HF2	125 kHz–16.125 MHz	n × 50 kHz; 1, 2, 4, or 8 linear channels within 25-kHz band	3.125, 6.25, 12.5, 25, or n × 50 kHz	10, 20, 40, or 80 ms

gain control (AGC) that provides a dynamic range of about 90 dB. In addition, a switchable attenuator provides an additional 26 dB of dynamic range. At any specific gain setting of the AGC, the digital spectrum analyzer has a dynamic range of about 30 dB. Table IV provides a summary of the basic characteristics of the high frequency receiver.

Using the two sets of receivers, complex auto- and cross-correlation measurements can be performed between the E_x dipole and E_w monopole antennas, thereby giving the amplitude and relative phase of signals detected by the two antennas. This mode of operation allows for polarization and direction-finding measurements of purely circularly polarized radio emissions such as cyclotron maser radiation. In an alternate mode of operation, the first of the two sets of receivers can be toggled rapidly between the E_u and E_v monopoles, with the second set on the E_w antenna, in order to provide direction-finding measurements.

For low frequency space-borne radio measurements, the wavelength λ is usually much larger than the length L of the antenna. Under these conditions ($\lambda >> L$) angular resolution is virtually nonexistent. Nevertheless, the direction to the center of the source can be obtained by comparing the amplitudes and relative phases of signals from various combinations of antennas. On a rotating spacecraft, direction-finding measurements can be performed with only two antennas. This technique was used by the Ulysses spacecraft to derive the location of Jovian low frequency radio sources with an accuracy of approximately 1–2° (Reiner *et al.*, 1993; Ladreiter *et al.*, 1994). The main limitation of the rotating antenna technique is that the radio emission characteristics must remain essentially constant during one spacecraft rotation, which usually takes 10 s or more. This is a serious limitation for auroral radio emissions, which often have rapid intensity variations, sometimes on time scales

of a fraction of a second or less. Such rapid variations explain why the technique could be applied to only limited portions of the Jovian radio spectrum (Ladreiter *et al.*, 1994). Since Cassini is three-axis stabilized the rotating antenna technique obviously cannot be used. Ladreiter *et al.* (1995) have shown that direction-finding and full polarization information (i.e., four Stokes parameters) can be obtained with three nearly orthogonal antennas. Direction-finding and polarization measurements are strongly interdependent parameters and, ideally, measurements should be made simultaneously on all three antennas. However, since the high frequency receiver can only process signals from two antennas at a time, direction-finding and polarization measurements are made using consecutive correlation measurements with two different pairs of antennas, (E_u, E_w) and (E_v, E_w). The time between these measurements is typically 45 to 325 ms (above 125 kHz) or 250 to 2000 ms (below 125 kHz). Because of the very short time interval between successive measurements, this technique is expected to be relatively insensitive to short-term intensity variations.

The high frequency receiver utilizes digital filters that have an out-of-band rejection greater than 45 dB. They are preceded by an anti-aliasing filter and an automatic gain control (AGC). The AGC normalizes the signal amplitude to a level that provides optimal performance for the digital signal processor. The first receiver has an input, which for simplicity we call E_1, that is selectable from either E_x, E_u, or E_v. The second receiver has an input, which we call E_2, from the E_w antenna. The digital processor provides two auto-correlations, $|E_1|^2$ and $|E_2|^2$, and two cross-correlation $\mathrm{Re}(E_1 \cdot E_2^*)$ and $\mathrm{Im}(E_1 \cdot E_2^*)$, for each frequency channel. In the normal mode of operation, a series of auto- and cross-correlation measurements is averaged in order to reduce fluctuations to the digital quantization level (1 bit = 0.375 dB). The exact number of spectrums integrated is controlled by command and depends on the detailed choices of frequency and bandwidth. The intrinsic noise level of the A, B, and C bands is 4.9×10^{-17} V^2 Hz^{-1} for the E_1 receiver and 2.5×10^{-17} V^2 Hz^{-1} for the E_2 receiver. For HF1 and HF2, these noise levels are typically double the A, B, and C noise levels due to mixer noise.

The high frequency receiver also has the capability of providing a frequency-converted signal to the wideband receiver. In the frequency conversion mode of operation, the high frequency receiver translates high frequency signals downward into a 50–75-kHz passband, which is then sent to the wideband receiver. This passband can be shifted to any frequency between 4.125 and 16 MHz, except those centered at multiples of 50 kHz, and to any frequency between 125 kHz and 4.125 MHz.

The high frequency receiver also includes a capability to measure amplitudes in a selected frequency channel with millisecond temporal resolution. In this mode of operation any frequency between 125 kHz and 16 MHz can be selected. This capability allows very short duration signals such as lightning to be detected and can be used for envelope sampling of bursty emissions.

TABLE V
Sounder transmission characteristics.

Band	Frequency range (kHz)	1/Pulse width (Hz)
1	3.6–7.2	200
2	7.2–14.4	400
3	14.4–28.8	800
4	28.8–57.6	1600
5	57.6–115.2	3200

Since the high frequency receiver is under the control of its own processor, virtually all of the receiver parameters can be selected by command, making for an extremely flexible instrument. This flexibility allows for regular surveys of the radio frequency spectrum of Saturn at low data rates (typically about 450 bps), as well as specialized studies of short duration phenomena at very high spectral resolution (the maximum number of frequency channels across the frequency range of the receiver is approximately 3300) as well as direction-finding and full polarization measurements. To minimize the data rate for a given mode, the processor also includes both lossless (Meander code) and lossy (Rice code) compression algorithms.

4.6. Sounder Transmitter

The high frequency receiver also includes a sounder transmitter. The transmitter design is based on the Ulysses/URAP instrument (Stone *et al.*, 1992). In the sounder mode of operation, a short pulse consisting of a 26-V peak-to-peak square wave is transmitted on the E_x dipole antenna, and the receiver then "listens" for a resonance response from the plasma. After each pulse the transmitter frequency is increased by a small increment. This process is continued across the entire frequency range of interest, thereby producing a spectrum of the plasma resonances. When a resonance is encountered, the received signal is strongly enhanced for a short period of time after the pulse has been transmitted. The sounder can measure electron densities from 0.2 to 164 cm^{-3} ($f_{pe} \approx 3.6$ to 115.2 kHz), and is expected to be active for a few seconds out of every 5 to 10 min.

The sounder can transmit in five bands over a frequency range from 3.6 to 115.2 kHz. The five bands are described in Table V. Each band is divided into 18 channels for a total of 90 frequencies. The default bandwidths are given in Table V. The upper and lower frequency limits of the frequency sweep can be selected by command.

Two modes of operation for the sounder are currently planned, designated PAA and AAA. Each of these two modes involves taking three measurements at the selected frequency. In the PAA (Passive Active) mode, a "passive" measurement is taken before the pulse is transmitted, and then two "active" measurements are

TABLE VI
Medium frequency receiver characteristics.

Band	Frequency range	$\Delta f/f$ (%)	Effective bandwidth (Hz)	Sweep time (s)
1	24–180 Hz	13	5.6	16
2	180 –1500 Hz	7	19.4	16
3	1.5–12 kHz	7	139	8

taken; the first at a time T_0 after the pulse, and the second at a time T_1 after the first measurement. In the AAA mode, three "active" measurements are taken sequentially at time intervals of T_0, T_1, and T_2 after transmission of the pulse. The parameters T_0, T_1, and T_2 can be selected by command.

4.7. Medium Frequency Receiver

The medium frequency receiver (MFR) system is based on similar receivers flown on the ISEE, Galileo, and Polar spacecraft (Gurnett *et al.*, 1978, 1992, 1995). The purpose of the medium frequency receiver is to provide continuous spectral measurements over a frequency range from 24 Hz to 12 kHz, with moderate frequency and temporal resolution and a relatively low data rate. This receiver system has the capability of processing signals from the B_x, B_z, E_u, E_v, E_w and E_x, antennas. In a typical mode of operation, the receiver toggles between the E_x dipole antenna and the B_x magnetic antenna in order to provide alternating electric and magnetic spectrums.

The medium frequency receiver consists of three frequency bands designated 1, 2, and 3, each covering a 3 octave frequency range. Band 1 is divided into 16 logarithmically spaced frequency channels ($\Delta f/f \simeq 13$ %) and bands 2 and 3 each have 32 frequency channels ($\Delta f/f \simeq 7$ %). The effective bandwidths for the three bands are given in Table VI. The frequencies are selectable using a two-stage frequency conversion scheme. Each band of the medium frequency receiver uses a mixer to convert the selected frequency to a fixed intermediate frequency (IF) filter. A second mixer then down-converts the IF signal to a baseband filter. The baseband signal is logarithmically compressed, rectified, and summed to provide a 0–5 volt DC output, and then converted to an 8-bit binary number by an analog-to-digital converter. The dynamic range of the medium frequency receiver, from the lowest signal that can be detected to the saturation level, is about 110 dB.

The upper frequency limits of the three medium frequency receiver frequency bands are determined by three bandpass filters at the front end of the receiver. The lower frequency limits are imposed by a combination of the bandpass filters and the low frequency limit of the front end (IF) mixer. The filter frequencies are scaled upward by a factor of eight for each successive higher band, thereby providing frequency coverage over nine octaves. The low-pass filters provide 55 dB of rejection for out-of-band signals.

TABLE VII
Waveform receiver input selections.

Channel	Input selection
1	E_x dipole, E_u*
2	E_w, E_v*
3	B_x, Langmuir probe*
4	B_y
5	B_z

*Operating in Langmuir probe (current collecting) mode.

4.8. Five-Channel Waveform Receiver

The five-channel waveform receiver provides simultaneous waveforms from up to five separate sensors in passbands of either 1 to 26 Hz, or 3 Hz to 2.5 kHz. The purpose of this receiver is to provide high-resolution spectral measurements and to determine the polarization and wave normal of low frequency plasma waves. When connected to the Langmuir probe (including the E_u and E_v monopoles operating in the current collecting mode), the waveform receiver can also provide $\delta n_e/n_e$ waveforms. The waveforms are sampled with 12-bit resolution once every 10 ms for the 1–26 Hz bands and once every 140 μs for the 26 Hz and 2.5 kHz bands. Simultaneous waveform samples from up to five receiver channels are stored in a buffer memory until they are read out via the science telemetry. The waveforms are processed on the ground to produce the auto- and cross-correlations that are needed to compute the wave normal and polarization.

The waveform receiver consists of five parallel analog input channels. The five inputs can be connected to various sensors. Table VII summarizes the sensor selections for each of the five channels. Signals from the five sensors are routed directly to a gain select stage that has commandable gains of 0, 10, 20, or 30 dB for each receiver channel. Channels 1 and 2 have independent gain settings, but channels 3–5 (which are usually connected to the B_x, B_y, and B_z magnetic sensors) share the same gain control lines. The programmable gain amplifiers are similar to those used in the wideband receiver. The amplifier gains are controlled by the high rate processor and can be operated in either a fixed gain mode or an automatic ranging mode. The output of the programmable gain amplifiers goes to a 26-Hz low-pass filter and a 3-Hz to 2.5-kHz bandpass filter. The desired analysis passband is selected by spacecraft command and the waveform outputs are sampled simultaneously by sample-and-hold circuits and converted to digital signals by a 12-bit analog-to-digital converter. The five-channel waveform receiver can also be commanded to measure one, two, three or four channels. These special modes allow greater resolution for special observations. For example, the single-channel waveform receiver mode using the 3-Hz to 2.5-kHz passband effectively allows

a third wideband receiver channel in addition to the 60-Hz to 10.5-kHz and 0.8–75-kHz channels that are included in the wideband receiver. Also, the waveform receiver provides signals to the digital processing unit in order to generate the passband for the low frequency receiver function (see Section 4.9).

Since the primary purpose of the five-channel waveform receiver is to provide the amplitude and relative phase of the five measured field components, each receiver channel must have known amplitude and phase responses. To achieve the required performance, all five low-pass passive filters have been carefully matched and are phase-stable to within a one degree between 1 Hz and 2.5 kHz.

4.9. Low Frequency Receiver

In order to have continuous spectral information in the frequency range from 1–26 Hz, waveforms from the five-channel waveform receiver are Fourier transformed by the data compression processor in the digital processing unit. The three-channel mode (E_x, E_w, B_x) of the five-channel waveform receiver is used, although typically only two of these channels, E_x and B_x, are analyzed, thereby providing simultaneous electric and magnetic spectrums. Processor speed limits the temporal resolution between successive spectrums to about 16 s. The Fourier transform processing utilizes a 512-point waveform to produce a 256-frequency component spectrum with 0.2-Hz resolution. To minimize the data volume and to produce a spectrum with resolution similar to that produced by the medium frequency receiver, the linear components of the spectrum are binned to form a logarithmically spaced spectrum with 32 frequencies covering a frequency range from 0.2 to 26 Hz.

4.10. Wideband Receiver

The wideband receiver is similar to the wideband receivers previously used on the Voyager, Galileo, Polar, and Cluster spacecraft, and provides high-resolution electric and magnetic field waveform measurements in passbands of either 60 Hz to 10.5 kHz, or 0.8–75 kHz. The wideband receiver also serves as the front end for the on-board dust detection function. The data compression processor (described below) is used to search the waveforms for the signature of dust impacts, based on those observed by the Voyager plasma wave instrument (see Figure 7).

The wideband receiver processes signals from a single selected sensor (either E_u, E_v, E_x, E_w, B_x, or Langmuir probe). To provide the capability for obtaining waveforms at higher frequencies, the wideband receiver input can be connected to the frequency conversion output from the high frequency receiver (see Section 4.5).

The instantaneous dynamic range of the wideband receiver is 48 dB. Because of the expected large dynamic range of the input signals, a set of discrete gain amplifiers and an automatic gain control are used to amplify the signal to the proper level in steps of 10 dB over a range of 0–70 dB. This system provides a total

dynamic range of over 100 dB for the wideband receiver. The feedback loop in the automatic gain control has a time constant of 0.1 s. However, gain updates are only made prior to a waveform capture. Since waveform captures typically occur once per multiple of 125 ms, the effective gain update can be much slower than 0.1 s. The output from the discrete gain amplifiers goes to the two bandpass filters (60 Hz to 10.5 kHz or 0.8–75 kHz). The output of the selected bandpass filter is sent to an 8-bit analog-to-digital converter. The sampling rate is 27,777 samples/s for the 10-kHz channel and 222,222 samples/s for the 75-kHz channel.

4.11. Data Processing Unit

The RPWS data processing unit uses three microprocessors, the low-rate processor (LRP), the high-rate processor (HRP), and the data compression processor (DCP), to perform the tasks necessary for the instrument operation. These processors are responsible for collecting the science and housekeeping data, data formatting and data compression, and provide the interface to the spacecraft command and data system.

The tasks and responsibilities of the three processors are as follows. The low-rate processor is considered the primary processor since it has the sole interface with the Cassini spacecraft via the bus interface unit (BIU). It also provides the interface to the high frequency receiver, the interface and control for the medium frequency receiver and the analog housekeeping analog-to-digital converter, and the control for the antenna motor subsystem. The high-rate processor is used to control the waveform and wideband receivers, and the Langmuir probe instrument. The high-rate processor contains a data compression chip for compression of waveform signals. The data compression processor contains a dedicated math processor and is used only for data processing tasks, such as data compression. This processor performs the on-board dust-detection and also the Fourier transforms for the low frequency receiver.

The essential elements of each of the three processors are an 80C85 microprocessor, two or more random access memory chips, and one or two read-only memory chips. The 80C85 runs with a 3-MHz clock and is used in the expanded configuration which uses an address latch to give a full 16-bit address bus and a bi-directional buffer to expand the data bus. Each processor can communicate with the other two processors via the interprocessor communication bus. The 80C85 has a memory address bus width of 16 bits giving a total addressing capability of 2^{16} or 64 kilobytes (kB). The memory in each of the processors consists of both a read-write memory and a read-only memory.

The low-rate and high-rate processors each have more than 64 kB of random access memory available. The low-rate processor contains 64 kB of read/write memory with 16 kB write-protected and 4 kB of read-only memory. The bus interface unit appears to the processor as an additional 16 kB of random access memory.

TABLE VIII
Summary of RPWS physical characteristics.

Element	Mass (kg)	Power (peak W)	Volume (cm^3)	Location
Main electronics	5.59	5.09	41.7 × 17.8 × 16.8	Main Bus, Bay 4
Antenna bracket assembly	29.77	11.14	61 × 67 × 67	Upper shell structure of Bay 4
Magnetic search coils	1.05	0	30 × 30 × 30	1-m boom attached to high gain antenna support structure
Magnetic search coil preamps	0.28	0.1	12.6 × 3.2 × 8.8	Base of search coil boom
Langmuir probe	0.85	0	74.3 × 10 × 11.5	0.8-m boom on search coil boom
Langmuir probe preamp	0.135	0.05	8.7 × 9 × 4.8	Base of search coil boom
Total	37.68	16.38		

The high-rate processor has 96 kB of random access memory. The excess memory is handled by switching memory chips under program and hardware control.

All communication with the spacecraft is over a redundant 1-MHz bi-directional serial data bus conforming to MIL STD 1553. The interface is implemented via a bus interface unit.

4.12. Mass, Power, and Telemetry

The RPWS has a total mass of 37.68 kg and requires a power of 16.38 W in its fully operational science modes. This power value does not include a momentary ∼3 W increase when the bus interface unit is active. By project policy, this bus interface power is allocated to the command and data system and not to the science instrument. Mass and power breakdowns for the various elements of the instrument are provided in Table VIII.

Because of its many different receivers, operating modes, and because of the use of several different data compression schemes, the RPWS has a highly variable science telemetry rate. In all of the defined telemetry modes that include RPWS science telemetry, there are four data pickup rates, or rates at which the RPWS can send data to the command and data system. These rates are 30.464, 60.928, 182.784, and 365.568 kbps. However, because of limitations on the Cassini solid state recorder data volume as well as limits on the total data volume that can be telemetered to the ground in any given day, the RPWS can utilize such high data rates only occasionally and for relatively short periods of time. Therefore, a number of different observing modes have been defined that use minimal data rates for basic survey information and utilize the higher data rates for special observations, usually

involving the wideband or five-channel waveform receivers. In the usual case where the actual science telemetry rate is less than the current telemetry mode's data pickup rates, RPWS outputs "zero-length" packets that are discarded by the command and data system to reduce the net data production rate.

The basic low-rate survey mode we have defined generates approximately 1 kbps before compression. Based on limited in-flight experience to date, the actual data rate in this mode after compression is about 700 bps. However, since most of the compression techniques used are data content dependent, it is not clear that this compressed data rate is representative of what will be encountered at Saturn. In addition to the continuous low-rate observations, the RPWS survey includes occasional wideband receiver samples (typically about one minute every couple hours) that are essential to the interpretation of the lower resolution data. On average, these high rate samples add approximately 600 bps to the RPWS survey rate. Typical observation modes that require higher data rates include the 75-kHz wideband receiver observations which generate close to 360 kbps before compression, the maximum duty cycle mode of the five-channel waveform receiver in the 2.5-kHz bandpass which generates approximately 130 kbps before compression, the low-duty cycle mode of the 10-kHz wideband receiver measurements which generates approximately 30 kbps before compression, and the high-resolution temporal and/or spectral modes of the high frequency receiver which generate data rates up to about 4 kbps.

Because of the uncertainty in the compression factors and data volume allocations imposed due to the limited downlink and onboard storage, the RPWS has the ability to monitor its actual data volume and compare it to a model. In the case where the actual data production is exceeding the model, various steps can be taken to decrease the data rate. For example, the rate at which waveform samples are acquired by the five-channel waveform receiver can be slowed down. This approach is effective when no wideband data are being acquired. During wideband receiver operations, the effective data rate can be reduced by decreasing the duty cycle of the wideband data. For example, instead of acquiring a 2048-sample data set once every 125 ms, a data set could be acquired every 250 ms.

5. Calibrations and Performance

An extensive series of amplitude calibrations, frequency responses, phase calibrations, and instrument performance checks were carried out on the RPWS prior to launch, both before and after integration on the spacecraft. These tests and calibrations were performed at room temperature (25 °C), –20 °C, and 40 °C. While there are calibration signals available in the instrument for in-flight calibration purposes, these are mainly used to check for drifts due to aging or radiation exposure. The

primary calibration information to derive physical units (spectral density, etc.) is derived from the prelaunch tests.

5.1. Calibration Procedure

5.1.1. *Electric Antennas*

Each of the RPWS electric antennas is connected to an amplifier located in the high frequency receiver. In the long wavelength regime where the wavelength is much greater than the tip-to-tip length of the antenna, L, the potential between the two elements of an electric dipole is given by $\Delta V = EL_{\text{eff}}$, where L_{eff} is a quantity called the effective length (Gurnett, 1998). This relation ignores the presence of any electrical load. For a dipole consisting of collinear elements, to a very good approximation L_{eff} is one-half the tip-to-tip length of the antenna. For a V configuration, L_{eff} is the distance between the geometric centers of the two elements. Taking into account the 120° included angle between the two elements of the E_{x} dipole and the finite distance between the roots of the two elements, the effective length of the Cassini E_{x} dipole is $L_{\text{eff}} = 9.26$ m. Next we must consider the effect of an electrical load on the antenna. At frequencies above a few tens of Hz, where the antenna impedance is primarily capacitive, the ratio of the output voltage to the input voltage is given by a simple capacitive divider,

$$\frac{V_{\text{out}}}{EL_{\text{eff}}} = \frac{C_{\text{A}}}{C_{\text{A}} + C_{\text{L}}}. \tag{1}$$

In the above equation C_{A} and C_{L} are the antenna and load capacities, respectively. For a cylindrical antenna, to a good approximation, the antenna capacity is given by

$$C_{\text{A}} = \frac{2\pi\varepsilon_0(L/2)}{[\ell n(L/2a) - 1]} \tag{2}$$

where $L/2$ is the length of the element, a is the radius of the element and ε_0 is the permittivity of free space. For $L/2 = 10$ m and $a = 0.014$ m, $C_A = 100.2$ pF.

TABLE IX

Measured base capacitances for the electric antennas.

	Base capacitance (pF)		
Contributor	E_u	E_v	E_w
Mechanism	50.4 ± 0.2	50.8 ± 0.2	50.7 ± 0.2
Coax cable	34.7 ± 0.3	34.3 ± 0.4	37.4 ± 0.4
HFR input	33.8	28.0	17.6
Total	118.9	113.1 ± 0.6	105.7 ± 0.6

The load capacity can be considered to be the sum of two parts: (1) the base capacity, which consists of the internal capacities of all circuits and mechanical structures connected to the base of the antenna; and (2) the capacity between the antenna and the spacecraft structure. Since the electric antenna cannot be fully extended to the in-flight configuration while the spacecraft is on the ground, there is no way to directly measure the capacitance between the antenna and the spacecraft structure. Thus, the total base capacitances listed in Table IX only give lower limits to the load capacities. Another, and perhaps better way to estimate the load capacities is to determine the half-wavelength resonance frequency of the antenna. This resonance frequency is shifted downward by a small amount due to the load capacity. During the instrument checkout in December 1998 and January 1999, a sharp peak was observed in the E_x dipole noise level at 8.5 MHz (see the discussion of noise levels in Section 5.2). This peak is due to the half-wave resonance. An antenna modeling program was then used with an accurate representation of the spacecraft geometry to determine the load capacitance required to place the resonant frequency at 8.5 MHz. The resulting value was $C_L = 150$ pF. This is our best current estimate of the load capacity for the E_x antenna. Using the capacitive divider relation above with $C_A = 100.2$ pF and $C_L = 150$ pF gives a loading loss of 7.9 dB for the E_x antenna.

Due to the complex shape of the Cassini spacecraft that acts as the ground plane for these antennas, the electrical axes of the antennas are expected to be rotated significantly from their physical orientations (Rucker *et al.*, 1996). Radio signals from Jupiter were used as a calibration source during the Cassini flyby of Jupiter in late 2000 and early 2001 to determine the electrical axes of the antennas. The orientations of the antenna axes can be determined by inverting the direction-finding software, using the direction to Jupiter as the source direction. Preliminary results from this calibration are given by Vogl *et al.* (2001). Additional antenna calibrations are scheduled on approach to Saturn and while in orbit after the Huygens probe is released.

Electric field calibrations of the receivers were performed by applying signals with known amplitudes at the preamplifier inputs and relating the input signal strength with the resulting telemetry value. As described below, the telemetry values from the various receivers are related to the input signal strength either via a set of look-up tables or through an analytical function that fits ground calibration data.

5.1.2. *Magnetic Antennas*

The sensitivity, frequency response, phase response, and noise levels of the magnetic search coil antennas were calibrated at a low-noise magnetic field observatory near Chambon La Foret, France. The calibrations were performed using a Helmholtz coil driven by a known AC current source to produce a magnetic field with a known magnitude and phase. The thermal blankets were installed in order to account for any conductivity effects that the blanket may have on the sensor response. The resulting data relate input field strength to the voltage at the magnetic preamplifier

output. Additional calibrations were then used to relate the voltage input to the various receivers to an output telemetry value. Combining these two steps provides an overall end-to-end calibration of the magnetic field measurements. This calibration was verified through a series of tests performed with the search coil antennas connected to the RPWS instrument after integration on the spacecraft. An end-to-end check of the phase response was also carried out after integration on the spacecraft. Noise levels were measured on the spacecraft by placing the search coils in a μ-metal chamber, which shields the sensors from external noise sources.

5.1.3. *High Frequency Receiver*

The calibration of the high frequency receiver was performed at Meudon, France. Sine wave and white noise sources with known spectral properties were applied to the input of the electric antenna amplifiers and the corresponding telemetry values were recorded. The calibration data were then fit to analytical models for each of the receiver bands. From these models, the telemetry values can be converted to physical units. A series of tests was then performed after integration of the instrument on the spacecraft, to verify the high frequency receiver calibrations.

5.1.4. *Medium Frequency Receiver*

The medium frequency receiver uses compressors with a piecewise-linear approximation to a logarithmic amplitude response. Over the range of amplitudes, the response of each compressor consists of a series of five distinct linear segments that deviate slightly from a true logarithmic response. Because the compressors for each of the three bands have different amplitude sensitivity characteristics, the amplitude response of each compressor must be measured separately. The amplitude response of a typical logarithmic compressor is shown in Figure 18 for channel 8 of Band 1 of the medium-frequency receiver. This curve was produced by applying a signal to the input of the electric antenna preamplifier at the center frequency of the filter (52.82 Hz). The amplitude was stepped in 2 dB increments to cover the complete amplitude range of the receiver. Similar amplitude responses were measured for Band 2 (channel 16) and Band 3 (channel 10).

Since all the frequency channels of a given medium frequency receiver band utilize the same logarithmic compressors, it is only necessary to measure the amplitude response at one frequency channel for each band. The amplitude responses for the remaining channels can be obtained by calibrating the gain through the entire system as a function of frequency at a fixed amplitude. This calibration is called a channel-to-channel gain test. By combining the amplitude response with the channel-to-channel gain calibration, a complete set of calibrated look-up tables can be produced that convert the output telemetry values to signal strengths at the preamplifier inputs.

The frequency response of the three filters used in the medium frequency receiver was also determined by sweeping a sine wave signal over frequency while monitoring the output of a fixed channel. Figure 19 illustrates responses of the single sideband filter for Band 1 and the double sideband filters for Bands 2 and 3 of the medium frequency receiver, as well as the center frequencies for each of the frequency steps in the receiver at the top of the figure.

5.1.5. *Low Frequency Receiver*

The low frequency receiver employs onboard fast Fourier transform processing of one or two channels of the five-channel waveform receiver to produce spectrums over a frequency range from 1 to 26 Hz. The calibration of the low frequency receiver involved both amplitude and frequency calibrations. The amplitude calibration is similar to the medium frequency receiver amplitude calibration. A signal was applied to the input of the electric antenna amplifier at the center frequency of every fourth Fourier frequency component. The amplitude was then stepped in 2 dB increments to cover the complete amplitude range of the receiver. Figure 20 shows the amplitude response of a typical low frequency receiver channel (channel 16). These tests were repeated for the various gain states, and at –20 °C and +40

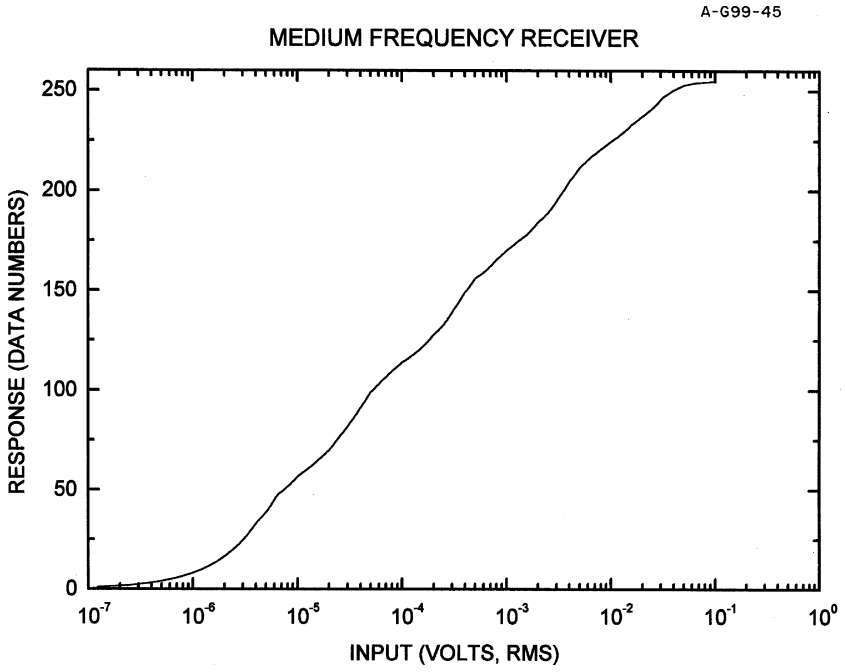

Figure 18. A typical medium frequency receiver calibration curve relating the input signal strength to the output of the log compressor. This particular curve is for the middle channel (channel 8) of the lowest frequency band (Band 1) of the receiver.

°C. The flattening of the curve at high input signal strength is due to saturation and the flattening at low input amplitudes is due to the preamplifier noise level.

The sensitivity of the low frequency receiver varies from channel to channel across the band. These frequency variations affect the calibration. A channel-channel gain test, similar to that performed on the medium frequency receiver, was conducted for each of the gain states of the low frequency receiver. This test was performed by applying an input signal of fixed amplitude to the input of the electric preamplifiers, and sweeping the signal from the lowest frequency channel of the low frequency receiver to the highest frequency channel. A combination of the amplitude response and the channel-channel gain measurements is then used to complete the calibration of the low frequency receiver for each gain state. Figure 21 shows the frequency response of the 32 quasi-logarithmically spaced channels. As discussed earlier, these channels are generated on board by binning (summing) Fourier components in such a way so as to create approximately logarithmically spaced channels.

5.1.6. *Wideband and Five-Channel Waveform Receivers*

The response of the wideband and five-channel waveform receivers was determined by applying signals of known frequency and amplitude to the electric preamplifiers, and determining the gain factors required to convert the telemetry values

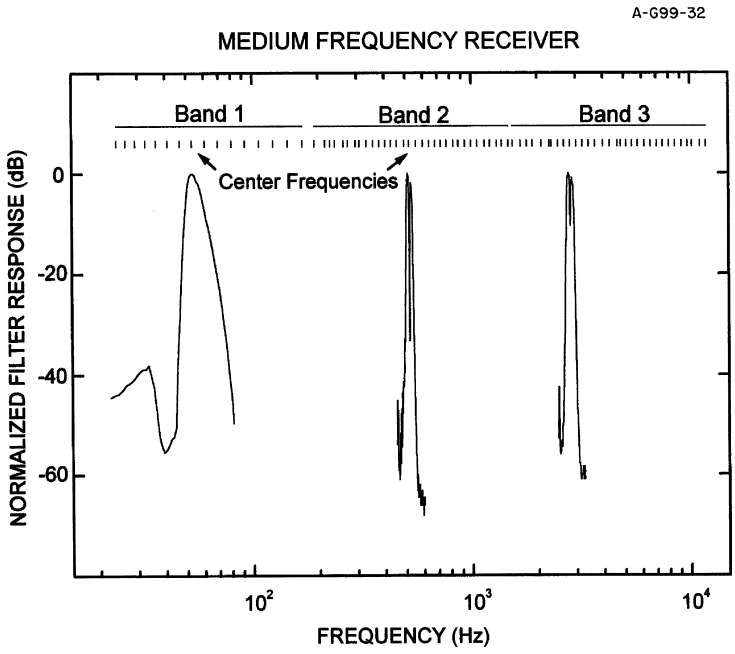

Figure 19. Frequency response curves and center frequency locations for the medium frequency receiver.

into physical units. These gain factors provide calibrations for both the time-series waveform and the spectrum produced by a Fourier transform of the waveform. The amplitude response of the wideband and five-channel waveform receivers was determined for each gain state, and for every filter mode. The frequency and phase response of the wideband receiver and the five-channel waveform receiver was determined by applying input signals of fixed amplitude to the input of the individual receivers, and sweeping the signal across the frequency band of the receiver. Figure 22 shows the frequency response of the two wideband receiver bands (10 and 75 kHz), and Figure 23 shows the frequency response of the 1–26-Hz and 3-Hz to 2.5-kHz bands of the five-channel waveform receiver. End-to-end calibration checks were performed by repeating the frequency response test and by applying an input signal of white noise with known spectral properties to the input of the electric and magnetic preamplifiers.

5.2. Performance

Cassini was successfully launched on 15 October 1997. At the time of this publication, the RPWS has been operated extensively during the cruise to Saturn: (1) for a period of about 30 h on 25–26 October 1997 in conjunction with the electric antenna deployment, (2) for about 2 h during the first Venus flyby on 26 April 1998 in a very limited mode designed to search for lightning, (3) for several days during

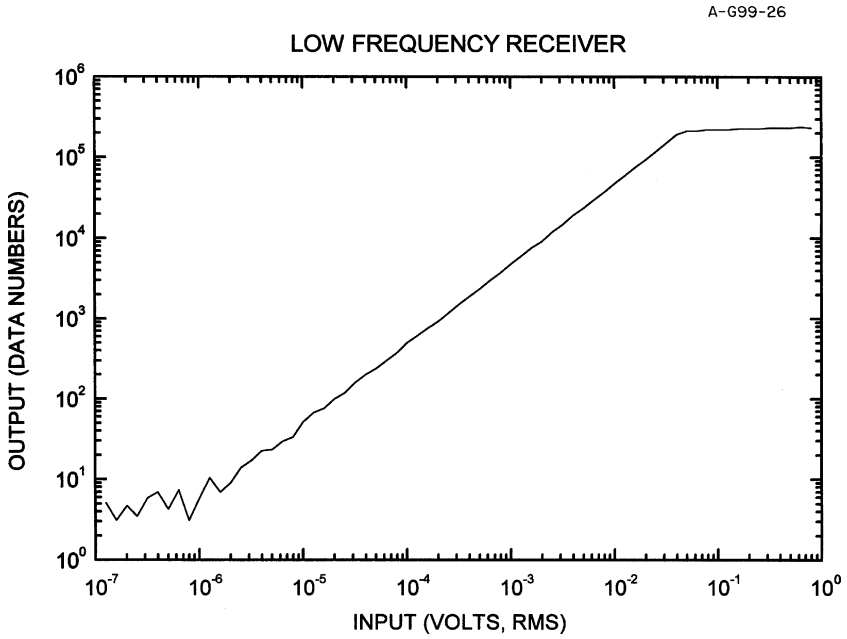

Figure 20. A typical low frequency receiver calibration curve relating the input signal strength to the output of the log compressor. This particular curve is for the 16th channel of the receiver.

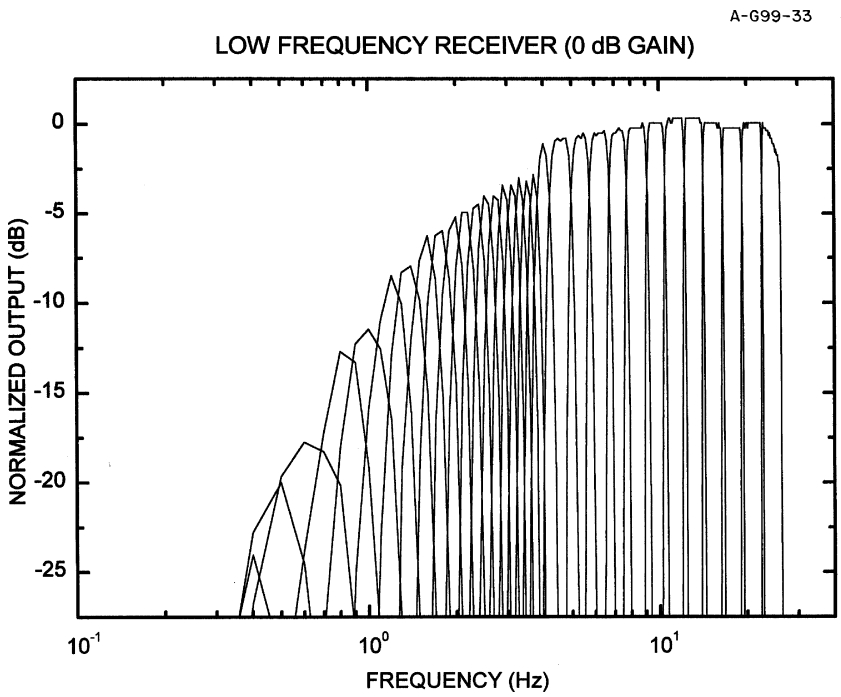

Figure 21. Frequency response curves for the quasi-logarithmically-spaced channels constructed on board from Fourier transform components for the low frequency receiver.

the period from 30 December 1998 to 19 January 1999 for instrument checkout, (4) for a few-hour period on 24 June 1999 during the second Venus encounter, (5) for about a month during the Earth flyby from 13 August to 14 September 1999, and (6) more-or-less continuously since February 2000 including a long period in the vicinity of Jupiter. The deployment data set was limited to modes designed to ensure that the electric antennas were properly deployed and provide some indication of in-flight performance. The first Venus flyby observations were of such a limited nature (28 channels between 80 kHz and 16 MHz) that they are not very useful for characterizing the in-flight operation of the instrument. The most complete data in hand are those from the instrument checkout and the Earth and Jupiter flybys. These data include a complete survey of noise levels obtained prior to other instruments being turned on as well as a limited quiet test which provided a first opportunity to observe any interference that might be generated by the spacecraft and other instruments. More importantly they provide extensive opportunities to study plasma waves in the solar wind and magnetospheric environments as well as a variety of solar and planetary radio emissions.

Figure 24 shows the noise levels from December 30, 1998 as observed on the E_x dipole, and Figure 25 shows the corresponding noise level on the B_x antenna.

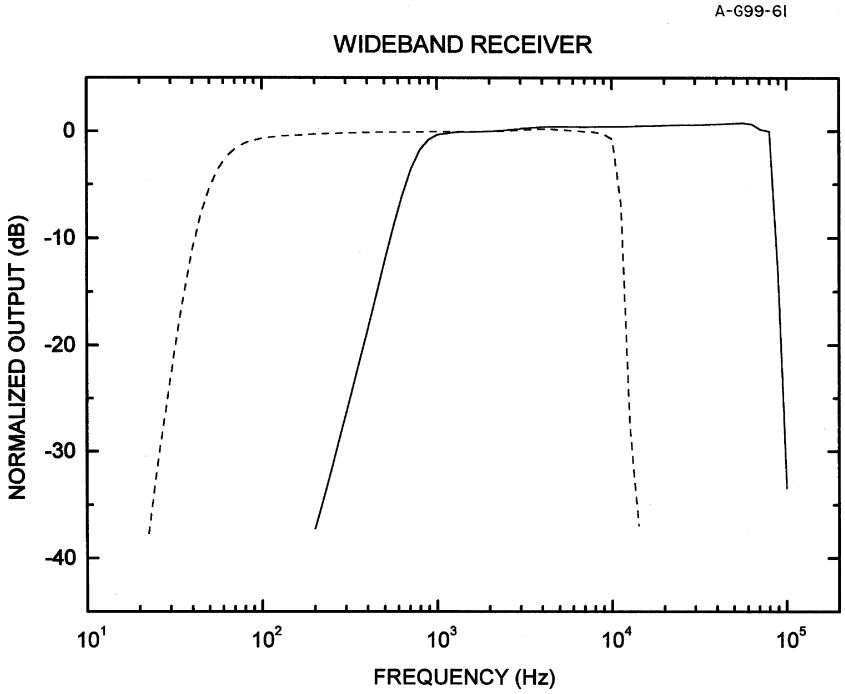

Figure 22. Frequency response curves for the 10- and 75-kHz wideband receiver filters.

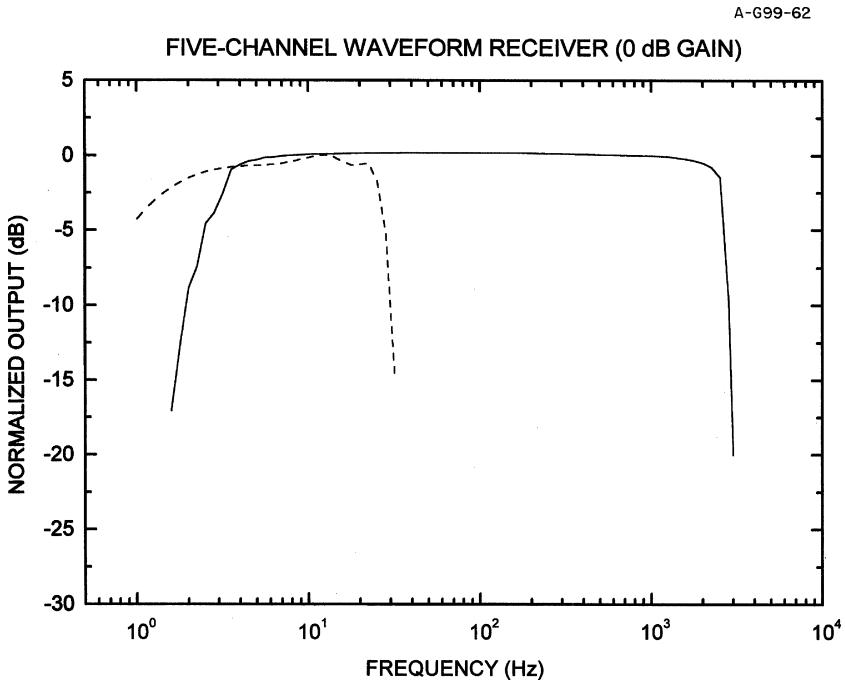

Figure 23. Frequency response curves for the 26-Hz and 2.5-kHz waveform receiver filters.

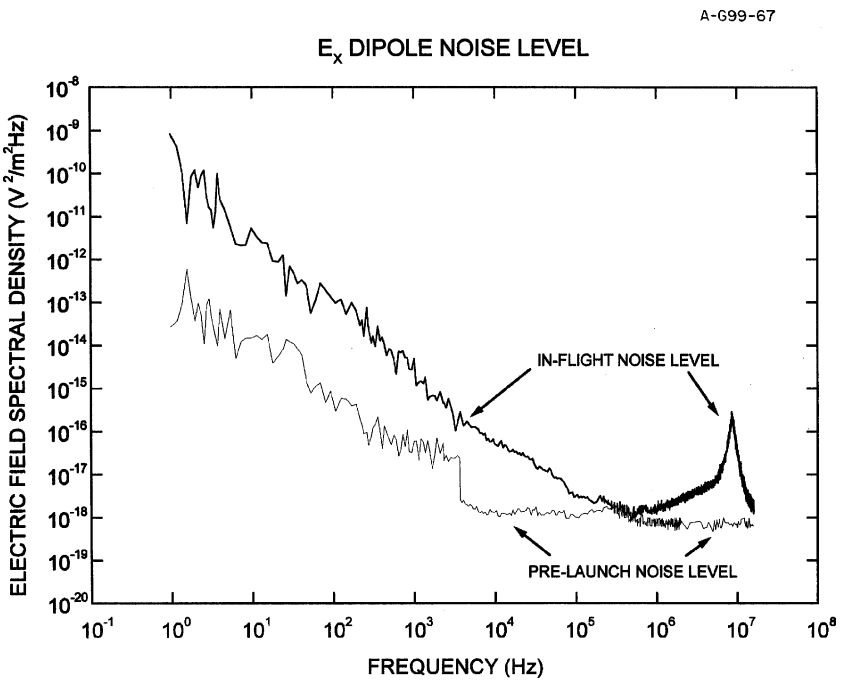

Figure 24. Plots of the pre-launch and in-flight noise levels for the E_x dipole antenna. The enhanced in-flight noise levels at low-frequencies (below about 10^5 Hz) is due to thermal plasma noise. The enhanced in-flight noise levels at high frequencies (above about 10^6 Hz) is due to galactic radio noise. The sharp peak in the noise level at about 8.5 MHz is due to the half-wavelength antenna resonance.

For comparison, the pre-launch noise levels are also shown. The in-flight magnetic noise levels are very similar to the pre-launch noise levels. The in-flight electric field noise levels appear to be significantly higher than the pre-launch noise levels, particularly at low frequencies. These elevated in-flight noise levels are mainly due to thermal plasma noise, which is a function of electron density and temperature and characteristics of the antenna such as its ratio of length to radius (Meyer-Vernet and Perche, 1989). At Saturn the thermal plasma noise levels are expected to be significantly lower because of the lower electron densities in the vicinity of Saturn. The enhanced in-flight noise levels at frequencies above about 1 MHz are due to the galactic background (Brown, 1973). The peak at 8.5 MHz is due to the half-wave resonance of the antenna. Comparisons with Ulysses and Wind observations indicate the sensitivity of the RPWS instrument compares favorably with the radio investigations on those spacecraft, even though they both employ significantly longer antennas than Cassini.

The performance of the RPWS during the cruise phase of the mission has been excellent. A number of examples of cruise data serve to illustrate this. Figure 26 shows an overview of the radio and plasma wave spectrum observed during the Earth flyby, which occurred on August 18, 1999 (Kurth *et al.*, 2001a). This spectrogram

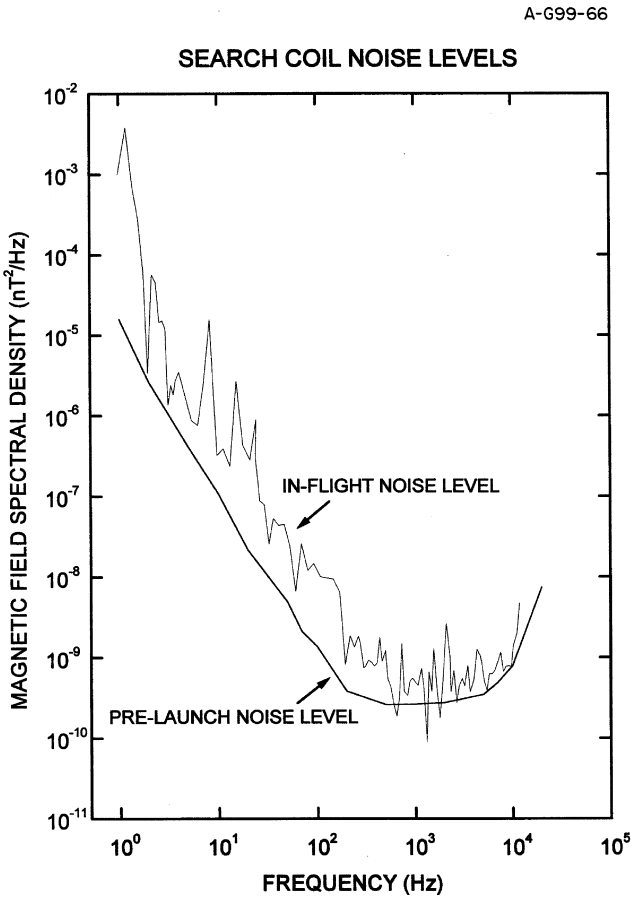

Figure 25. Plots of the pre-launch and in-flight noise levels of the search coil magnetic sensor. The slightly enhanced in-flight noise levels below about 100 Hz are believed to be due to a combination of spacecraft-generated interference (the sharp spikes) and solar wind plasma waves.

shows solar, terrestrial, and man-made radio emissions at the highest frequencies as well as the significant boundaries of the terrestrial magnetosphere and many of the plasma wave modes normally found within it. During the Earth flyby the instrument was configured to obtain intensive observations in the 2.5-kHz waveform receiver mode and subsequent analyses of chorus and other terrestrial plasma wave phenomena have demonstrated the use of this receiver for wave normal and Poynting flux analyses (Hospodarsky *et al.*, 2001). Also during the Earth flyby, both the sounder and Langmuir probe were successfully operated in the magnetospheric conditions for which they were designed. As shown in Kurth *et al.* (2001a) both portions of the instrument functioned well and returned excellent electron density information.

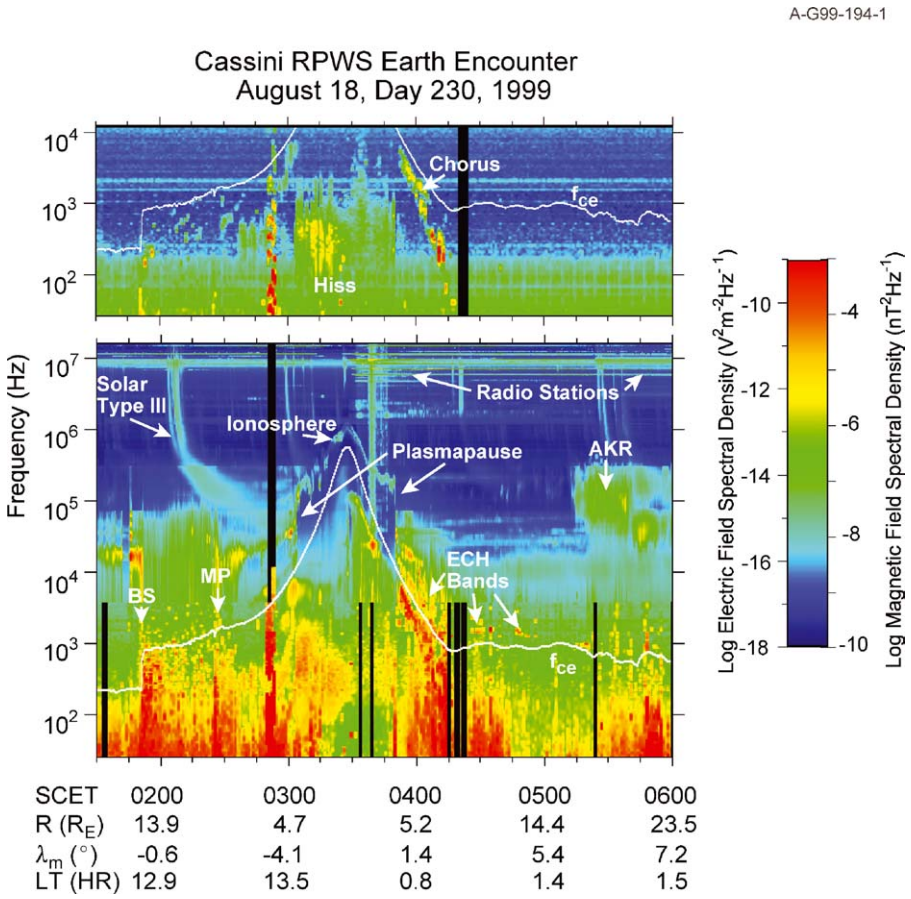

Figure 26. An overview of radio and plasma wave phenomena observed during the Earth flyby (Kurth *et al.*, 2001a). The upper panel shows magnetic fields and the lower panel the electric fields. Noted in the illustration are various boundaries of the magnetosphere (BS: bow shock and MP: magnetopause) as well as the primary emissions identifiable at the resolution of these spectrograms. The burst of noise at about 0250–0255 is due to a high duty-cycle sounder test and does not represent a natural emission. Normal sounder operations will occur on a much lower duty cycle and should not be as disruptive.

The high frequency receiver's capabilities have also been demonstrated in flight. Figure 27 shows examples of many of the various types of Jovian radio emissions as observed during the Jupiter flyby in late 2000 (Gurnett *et al.*, 2002; see also Lecacheux, 2001). The sensitivity and noise characteristics of the high frequency receiver are evident in this display. Pending completion of the analysis of the Jupiter antenna calibration, it appears that the polarization and direction-finding capabilities of this receiver will also be shown to be as designed (Lecacheux, 2001). The high and medium frequency receivers were used in new studies of the influence of the solar wind on the Jovian magnetosphere (Gurnett *et al.*, 2002; Kurth *et al.*, 2002).

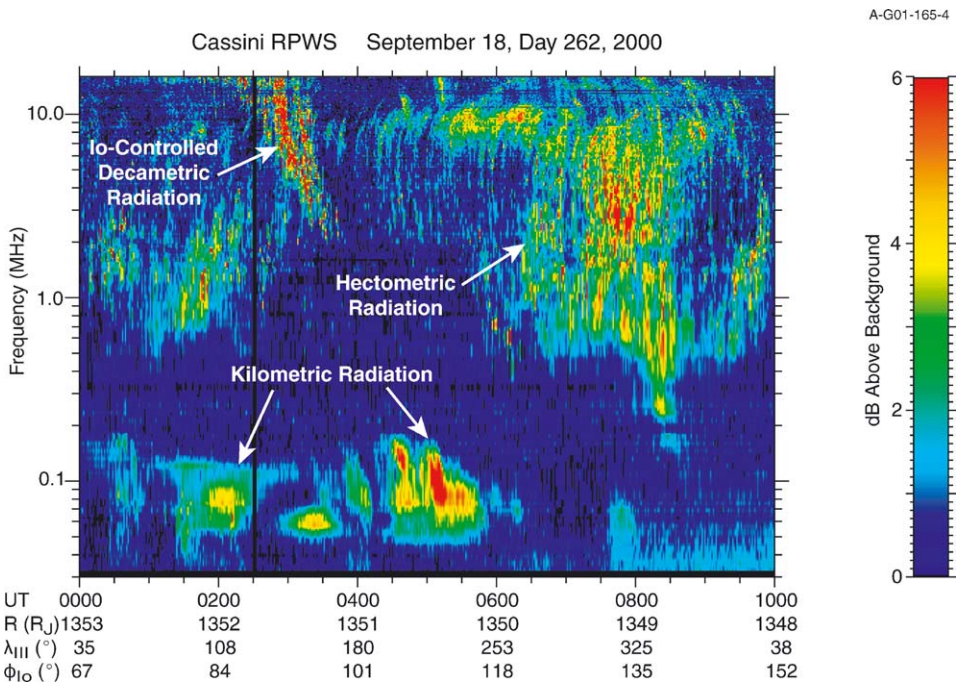

Figure 27. Observations of many of the various types of Jovian radio emissions (Gurnett *et al.*, 2002). This spectrogram shows examples of decametric, hectometric, and kilometric radiation during one Jovian rotation. Although the spacecraft is two-thirds of an AU from Jupiter at the time, there is considerable signal-to-noise ratio for all of the emissions and clear evidence of the arc-like structures which comprise the decametric and hectometric emissions.

The Jupiter flyby also provided a unique opportunity to study the fine temporal and spectral detail of a number of Jovian radio emissions for the first time using the capabilities of both the wideband receiver and the high frequency receiver (Kurth *et al.*, 2001b; Lecacheux *et al.*, 2001; Kaiser *et al.*, 2001).

Figure 28 displays the first confirmed detection of Saturn in the RPWS data while Cassini was at a distance of greater than 2.5 AU from Saturn. A high-density region in the solar wind was detected at 1 AU and ballistically propagated radially to determine when the region would pass by Jupiter and Saturn. Within a day or so of the predicted time, low frequency Jovian radio emissions were clearly observed by Cassini. Subsequently, and again within a day or so of the ballistic propagation, evidence of the arrival of the high density region at Saturn was marked by the detection of the radio emissions shown in Figure 28 by Cassini. Given this expected response of SKR in response to the arrival of a high density solar wind at Saturn and the similarity in spectrum and temporal variability to SKR observed by Voyager, we are confident that these emissions are, indeed Saturn kilometric radiation. A number of other examples of SKR are also present in the RPWS

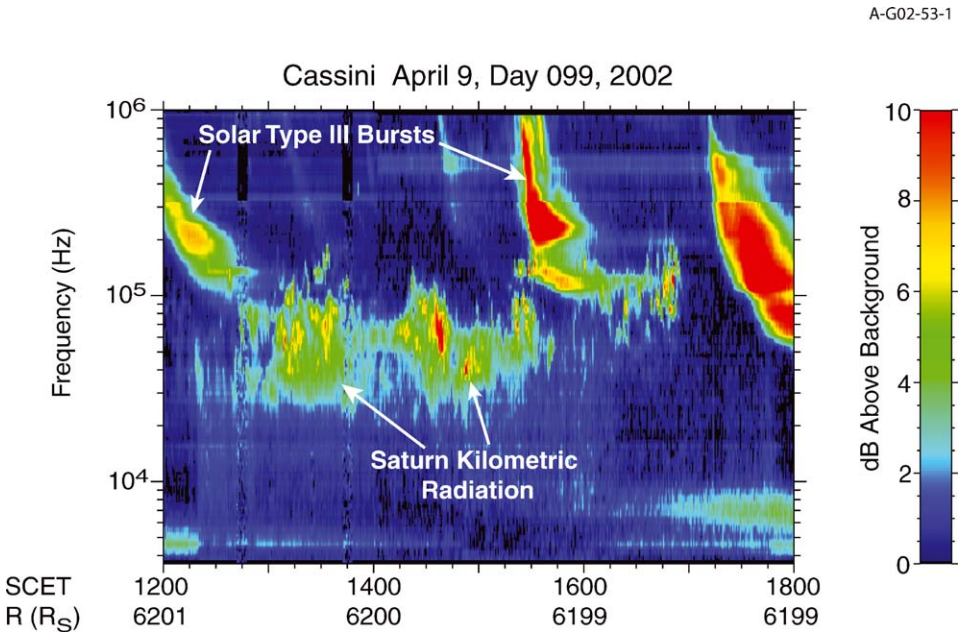

Figure 28. One of the first confirmed detections of Saturn kilometric radiation made while Cassini was still 2.5 AU from Saturn. The Saturnian emissions extend from about 30 to 200 kHz in this example and last for several hours. This radio activity is thought to be the result of a high-density region in the solar wind interacting with Saturn's magnetosphere.

measurements from early 2002, onward. Hence, it is clear that Cassini's study of the Saturnian magnetosphere and its response to the solar wind input is well under way.

6. In-Flight Operations, Data Processing, and Archiving

As can be seen from the preceding description, the RPWS instrument is quite complex and has a number of different operating modes. This complexity has a strong impact on the in-flight operation of the instrument and on the analysis and archiving of the data. In this section we provide an overview of the instrument operations, data analysis, and data archiving.

6.1. In-flight Operations

The different types of receivers used to cover the spectral and temporal range covered by the RPWS does not lend itself to a monolithic, synchronous mode of operation. Nevertheless, to reduce the magnitude of the in-flight operations to an acceptable level requires that many of the measurements be scheduled in a systematic way. The approach is to attempt to acquire survey information in the form of uniform spectral and temporal information at a low enough data rate, $\sim$1 kbps, to

ensure that such coverage is available for the entire Saturnian tour and for a large portion of the cruise and approach to Saturn. The survey data set will support spatial mapping, statistical studies, and studies of dynamical effects in the magnetosphere and their possible correlation with solar wind variations. In addition to the survey information, special observations will be added (sometimes at greatly increased data rates) at specific locations or times to provide enhanced information required by several of the science objectives. The special observations may include full polarization and direction-finding capability or high spectral or temporal resolution observations by the high frequency receiver, wideband measurements at one of the possible bandwidths, acquisition of $\delta n_e/n_e$ measurements, or intensive wave-normal analysis afforded by acquiring five-channel waveforms on an accelerated schedule. While minimizing the number of different modes in which the instrument is operated both simplifies operations and yields a more manageable data set, flexibility (for example in the duty cycle of wideband measurements) increases the likelihood that enhanced measurements can be integrated successfully with the resource requirements of the other instruments. One of the resources which will be most limited on Cassini is the overall data volume; RPWS requires large data volumes for some of its measurements.

To simplify operations and to be consistent with Cassini Project policies, virtually all RPWS observational modes are defined by internal sequencing constructs termed instrument expanded blocks. In the RPWS, an instrument expanded block is, in essence, a small subroutine that sets up each of the receivers as required for the desired mode. In some cases, the instrument expanded block cycles the instrument through a small number of modes having a relatively short cycle period with each step in the cycle lasting several seconds to several minutes. Each observation mode, then, is initiated by a trigger command. In most cases, the instrument will continue operating in the triggered mode until another trigger command is received which initiates the next desired mode. Early in the tour, it is anticipated that the set of instrument internal blocks will change with each background sequence load (approximately once per month). However, it is possible and desirable that the required set of instrument expanded blocks will stabilize with flight experience and each sequence later in the tour will only require a new set of trigger commands using the established "library" of modes.

The RPWS team has provisionally defined a small number of observation modes to date and these have been exercised in a very limited way in flight. Here, we illustrate a few of these modes.

Survey Mode: The survey mode is designed to acquire basic information on a continuous basis from all of the RPWS receivers with low to moderate temporal and spectral resolution at a low data rate in order to support many of the scientific objectives of the investigation, most notably those dealing with the configuration of the magnetosphere and its dynamics. The survey data also provide context for more intensive measurements at specific times and locations such as satellite flybys. This mode acquires one electric field and one magnetic field spectrum every

16 and 32 s in the low and medium frequency receivers, respectively, covering the range from 1 Hz to 12 kHz and collects 180 channels between 3.5 kHz and 16 MHz with the high frequency receiver once per 16 s. Approximately once per two and one-half minutes, a set of five-channel waveforms is acquired. The waveform alternate between the low (26 Hz) and high (2.5 kHz) band so that waveforms in both bands are acquired approximately once every five minutes. Waveform samples are acquired from the E_w antenna once every 5 s and analyzed onboard for signatures of dust impacts based on algorithms used to identify impacts in the Voyager plasma wave waveform data. The sounder is operated for a few seconds every five or ten minutes and the Langmuir probe is swept every five minutes, 40 s and density measurements at fixed bias are acquired every 16 s in between sweeps. The data rate for this mode is about 700 bps, after compression. In addition to these low rate measurements, a cyclic (repeating) activity will run with a periodicity of about two hours that will acquire a $\sim$1 min set of wideband data each cycle. Beyond about 15 R_S the wideband data will be in the 10-kHz mode. Inside of this distance, brief samples will be acquired in both the 10- and 75-kHz modes. The long-term average data rate of these wideband samples is approximately 600 bps, after compression.

Wideband Mode: This mode adds to the Survey Mode the acquisition of intensive wideband data in either the 10- or 75-kHz bandwidth for extended periods of time (several minutes to a few hours) with a duty cycle that is commensurate with the data volume allocated for the measurement. A high duty cycle mode would acquire 2048-sample waveforms every 125 ms with an uncompressed data rate of about 131 kbps. This mode would be used, for example, to study the detailed spectral and temporal character of whistler-mode chorus. The duty cycle is decreased by acquiring 1 of every n possible 2048-sample data sets. Duty cycling employed in this manner retains the spectral resolution afforded by the 2048 contiguous samples, but sacrifices the temporal resolution between the data sets in order to minimize the data rate. One specific use of this duty-cycled wideband mode is to acquire waveforms from the E_w antenna at ring plane crossings to determine the thickness and scale height of the E ring. The elevated impact rates during ring plane crossings will not likely be handled well with the onboard dust detection algorithm, hence, acquiring the waveforms for analysis on the ground is required.

Other Modes: Other, more specific modes will be developed during cruise which will be used for special observations. For example, during campaigns designed to study the interactions of the rings and icy satellites with the magnetosphere, a modified version of the survey mode that increases the rate of waveform captures will enable a more intensive examination of waves associated with ion pickup. During traversals through the high latitude, low altitude regions later in the tour when it is possible that auroral field lines would be crossed, wideband and/or waveform data will be acquired on an enhanced schedule that will permit the identification of electrostatic solitary structures. The high frequency receiver will also be reconfigured

to support observations near the source of Saturn kilometric radiation by increasing spectral or temporal resolution or by focusing on the direction-finding capabilities of the receiver.

6.2. Data Processing

The RPWS team is large and spans several institutions. Also, since hardware is provided by a number of different institutions, the expertise for different portions of the instrument resides at different institutions. This situation requires a distributed data analysis approach. However, the desire to make data and analysis results available to all team members and the need to ensure that the results of a given analysis are uniform, no matter where the analysis takes place, present a particular challenge. Our approach to this challenge involves a number of elements.

First, the basic data products will be produced in a centralized fashion at The University of Iowa. This is primarily dictated by the fact that the project supplies a single data port per principal investigator and this port is located at the principal investigator's home institution. All raw telemetry packets and ancillary data such as ephemeris and attitude information will be collected at The University of Iowa. The raw telemetry packets will be edited and decompressed (where necessary) and stored in a small number of file types whose format is agreed to by the team. It is anticipated that these same file types will be directly archivable with the planetary data system (PDS) with the appropriate labels and documentation. The resulting files will be stored both at The University of Iowa and CETP in France. The two databases ensure easy access to both U.S. and European co-investigators and also provide a level of security against loss.

Second, the institution responsible for providing specific hardware (see Table I) will provide algorithms and look-up tables as required to convert the telemetry values into physical units. These calibration algorithms and look-up tables will be maintained in the RPWS calibration documentation developed under the direction of the principal investigator. Hence, any changes in calibrations will be propagated to the team in a well-controlled manner.

Third, the cognizant institutions will also develop analysis tools and distribute these to other team members, as requested. The most generic of these tools, i.e., those providing general analysis and display capabilities of interest to many team members, will be accessible through a web-based system located at The University of Iowa (and perhaps mirrored at a location in Europe). Such a system will make the tools available to the widest set of investigators without requiring that the software be ported to numerous computing platforms. More specific analysis tools, needed for highly specialized analyses, will likely reside only in the institutions where they were developed. Results from these more specialized tools will be available to all team members and will be archived with the planetary data system as high-level data sets.

6.3. ARCHIVING

The RPWS team intends to provide a complete archive to the PDS, consistent with the Cassini Project and PDS requirements. The University of Iowa is the outer planets subnode of the planetary plasma interactions node of the PDS, which should ensure the timely archive of data with compliant formats. Currently, several different types of archive data sets are envisioned. The basis of the RPWS archive will be a full-resolution, calibrated data set (CODMAC Level 3) with documentation. High volume data sets including wideband and waveform receiver data will be archived in uncalibrated, edited telemetry format (CODMAC Level 2) with calibration tables and procedures. This approach is dictated by the already large data volumes of these data sets.

A browse data set will also be archived. This data set will be a fully calibrated set of amplitudes as a function of frequency and time but at somewhat lower resolution than that ultimately achievable by the instrument. This data set will enable quick and easy access to the RPWS data in order to search for events or to support high level surveys of the data.

It is also likely that a number of highly specialized data sets will be archived after significant detailed analyses. Examples of such data sets include the results of the Langmuir probe measurements and radio direction-finding results. Plans for these highly specialized archives will evolve over time.

Acknowledgements

The authors would like to express their thanks to R. Barrie, R. Brechwald, A. Cooper, M. DeBower, R. Huff, R. Johnson, S. Kutcher, M. Mitchell, B. T. Pham, J. Phillips, R. Randall, S. Remington, W. Robison, W. Schintler, J. Schwartz, P. Sheyko, D. Tomash, and E. Williams at the University of Iowa, for their role in designing, assembling, and testing the instrument; to P. Fédou, N. Monge, D. Carriere, J. M. Boulben, R. Knoll, J. P. Mengue, C. Gueriau, L. Belmon, G. Nicol, A. Rapin, and L. Friel at the Observatoire de Paris, for their role in designing, assembling, and testing the high frequency receiver; to P. Chauveau and S. Louis at CETP, for their role in designing, assembling, testing of the search coil magnetic sensors, and to V. Bouzid for her role in software development; to H. Gunnarsson, B. Holback, S.-E. Jansson, and H. Thomas at the Swedish Institute of Space Physics, for their role in designing, assembling, and testing the Langmuir probe; to I. Willis at the University of Sheffield, for his role in the software development; to R. Kramer of Orbital Sciences Corporation for his role in constructing the electric antennas; to W. Fawcett, K. Breitenbach, M. Lane, R. Poynter, P. Liewer, and S. J. Bolton at the Jet Propulsion Laboratory for their role in coordinating the experiment integration and testing at the Jet Propulsion Laboratory. Special thanks are also given to R. Spehalski, R. Draper, T. Gavin, and E. Miner at the Jet Propulsion Laboratory for their help in solving many of the spacecraft interface problems associated

with a complex instrument of this type. The U.S. funding for the instrument development, assembly, and testing was provided by NASA through contract 959515 through the Jet Propulsion Laboratory. The post-launch U.S. mission operations and data analysis phase of this investigation is supported by NASA through contract 961152, also through the Jet Propulsion Laboratory. The Observatoire de Paris contributions were supported by the Centre National d'etudes Spatiales. The CETP contributions are supported by Centre National d'etudes Spatiales under contract 204.

References

Aubier, M. G., Meyer-Vernet, N., and Pedersen, B. M.: 1983, *Geophys. Res. Lett.* **10**, 5–8.

Benson, R. F.: 1970, in: Thomas, J. O., and Landmark, B. J. (eds.), *Plasma Waves in Space and Laboratory, 2,* Edinburgh University Press, Edinburgh, pp. 25–54.

Blanc, M., Bolton, S., Bradley, J., Burton, M., Cravens, T. E., Dandouras, I., Dougherty, M. K., Festou, M. C., Feynman, J., Johnson, R. E., Gombosi, T. G., Kurth, W. S., Liewer, P. C., Mauk, B. H., Maurice, S., Mitchell, D., Neubauer, F. M., Richardson, J. D., Shemansky, D. E., Sittler, E. C., Tsurutani, B. T., Zarka, P., Esposito, L. W., Gruen, E., Gurnett, D. A., Kliore, A. J., Krimigis, S. M., Southwood, D., Waite, J. H., and Young, D. T.: 2002, *Space Sci. Rev.*, **104**, 253–346.

Bougeret, J.-L., Kaiser, M. L., Kellogg, P. J., Manning, R., Goetz, K., Monson, S.J., Monge, N., Friel, L., Meetre, C.A., Perche, C., Sitruk, L., and Hoang, S.: 1995, *Space Sci. Rev.* **71**, 231.

Brown, L. W.: 1973, *Astrophys. J.* **180**, 359–370.

Burns, J. A., Showalter, M. R., Cuzzi, J. N., and Durisen, R. H.: 1983, *Icarus* **54**, 280–295.

Cairns, I. H., and Melrose, D. B.: 1985, *J. Geophys. Res.* **90**, 6637–6640.

Carr, T. D., Desch, M. D., and Alexander, J. K.: 1983, in: Dessler, A. J. (ed.), *Physics of the Jovian Magnetosphere*, Cambridge University Press, Cambridge, pp. 226–284.

Decreau, P. M., Hamelin, E. M., Massif, R., DeFeraudy, H., Pawela, E., Perraut, S., Pottelette, R., and Bahnsen, A.: 1987, *Ann. Geophys.* **5A**, 181–185.

Desch, M. D.: 1982, *J. Geophys. Res.* **87**, 4549–4554.

Desch, M. D., and Kaiser, M. L.: 1981, *Geophys. Res. Lett.* **8**, 253–256.

Desch, M. D., and Kaiser, M. L.: 1990, *Nature* **343**, 442–444.

Ergun, R. E., Carlson, C. W., McFadden, J. P., Delory, G. T., Strangeway, R. J., and Pritchett, P. L.: 2000, *Astrophys. J.* **538**, 456–466.

Esposito, L. W., Cuzzi, J. N., Holberg, J. B., Marouf, E. A., Tyler, G. L., and Porco, C. C.: 1984, in: Gehrels, T. and Matthews, M. S. (eds.), *Saturn*, University of Arizona Press, Tucson, pp. 463–545.

Etcheto, J., and Bloch, J. J.: 1978, *Space Sci. Rev.* **22**, 597–610.

Etcheto, J., Belmont, G., Canu, P., and Trotignon, J. G.: 1983, *Eur. Space Agency Spec. Publ.* **SP-195**, 39–46.

Galopeau, P., and Zarka, P. 1992, Reply to the comment by J. E. P. Connerney and M. D. Desch, *J. Geophys. Res.* **97**, 12,291–12,297.

Galopeau, P. H. M., and Lecacheux, A.: 2000, *J. Geophys. Res*. **105**, 13089–13101.

Galopeau, P., Zarka, P., and Le Queau, D.: 1989, *J. Geophys. Res.* **94**, 8739–8756.

Galopeau, P., Ortega-Molina, A., and Zarka, P.: 1991, *J. Geophys. Res.* **96**, 14,129–14,140.

Galopeau, P., Zarka, P, and Le Queau, D.: 1995, *J. Geophys. Res.* **100**, 26,397–26,410.

Goertz, C. K., and Morfill, G. E.: 1983, *Icarus* **53**, 219–229.

Goldreich, P., and Lynden-Bell, D.: 1969*, Astrophys. J.* **156**, 59–78.

Goldstein, M. L., and Goertz, C. K.: 1983, in: Dessler, A. J. (ed.), *Physics of the Jovian Magnetosphere,* Cambridge University Press, pp. 317–352.
Grün, E.: 1981, *Eur. Space Agency Spec. Publ.* **SP-155**, 81–90.
Grün *et al.*, this issue.
Gurnett, D. A.: 1974, *J. Geophys. Res.* **79**, 4227–4238.
Gurnett, D. A.: 1998, in: Pfaff, R. F., Borovsky, J. E., and Young, D. T. (eds.), *Measurement Techniques in Space Plasmas: Fields, Geophys. Monograph 103,* American Geophysics Union, Washington, DC, pp. 121–136.
Gurnett, D. A., and Shaw, R. R.: 1973, *J. Geophys. Res.*, **78**, 8136–8149.
Gurnett, D. A., Scarf, F. L., Fredricks, R. W., and Smith, E. J.: 1978, *IEEE Trans. Geosci. Electron.* **GE-16**, 225–230.
Gurnett, D. A., Anderson, R. R., Scarf, F. L., Fredricks, R. W., and Smith, E. J.: 1979a, *Space Sci. Rev.* **23**, 103–122.
Gurnett, D. A., Shaw, R. R., Anderson, R. R., and Kurth, W. S.: 1979b, *Geophys. Res. Lett.* **6**, 511–514.
Gurnett, D. A., Kurth, W. S., and Scarf, F. L.: 1981, *Science* **212**, 235–239.
Gurnett, D. A., Grün, E., Gallagher, D., Kurth, W. S., and Scarf, F. L.: 1983, *Icarus* **53**, 236–254.
Gurnett, D. A., Kurth, W. S., Scarf, F. L., Burns, J. A., Cuzzi, J. N., and Grün, E.: 1987, *J. Geophys. Res.* **92**, 14,959–14,968.
Gurnett, D. A., Kurth, W. S., Cairns, I. H., and Granroth, L. J.: 1990, *J. Geophys. Res.* **95**, 20,967–20,976.
Gurnett, D. A., Kurth, W. S., Granroth, L. J., and Allendorf, S. C.: 1991, *J. Geophys. Res.* **96**, 19,177–19,186.
Gurnett, D. A., Kurth, W. S., Shaw, R. R., Roux, A., Gendrin, R., Kennel, C. F., Scarf, F. L., and Shawhan, S. D.: 1992, *Space Sci. Rev.* **60**, 341–355.
Gurnett, D. A., Persoon, A. M., Randall, R. F., Odem, D. L., Remington, S. L., Averkamp, T. F., DeBower, M. M., Hospodarsky, G. B., Huff, R. L., Kirchner, D. L., Mitchell, M. A., Pham, B. T., Phillips, J. R., Schintler, W. J., Sheyko, P., and Tomash, D. R.: 1995, *Space Sci. Rev.* **71**, 597–622.
Gurnett, D. A., Kurth, W. S., Roux, A., Bolton, S. J., and Kennel, C. F.: 1996, *Nature* **384**, 535–537.
Gurnett, D. A., Zarka, P., Manning, R., Kurth, W. S., Hospodarsky, G. B., Averkamp, T. F., Kaiser, M. L., and Farrell, W. M.: 2001, *Nature* **409**, 313–315.
Gurnett, D. A., Kurth, W. S., Hospodarsky, G. B., Persoon, A. M., Zarka, P., Lecacheux, A., Bolton, S. J., Desch, M. D., Farrell, W. M., Kaiser, M. L., Ladreiter, H.-P., Rucker, H. O., Galopeau, P., Louarn, P., Young, D. T., Pryor, W. R., and Dougherty, M. K.: 2002, *Nature* **415**, 985–987.
Hanel, R. A., Conrath, B. J., Flasar, F. M., Kunde, V. G., Maguire, W., Pearl. J. C., Pirraglia, J. A., Samuelson, R., Hearth, L., Allison, M., Cruikshank, D. P., Gautier, D., Gierasch, P., Horn, L., Koppany, R., and Ponnamperuna, C.: 1981, *Science* **212**, 192–200.
Harvey, C. C., Etcheto, J., and Mangeney, A.: 1979, *Space Sci. Rev.* **23**, 39–58.
Hornung, D. H., and Draptz, S.: 1981, *Eur. Space Agency Spec. Publ.* **SP-155**, 23.
Hospodarsky, G. B., Averkamp, T. F., Kurth, W. S., Gurnett, D. A., Dougherty, M., Inan, U., and Wood, T.: 2001, *J. Geophys. Res*. **106**, 30,253–30, 269.
Hunten, D. M., Tomasko, M.G., Flasar, F. M., Samuelson, R. E., Strobel, D. F., and Stevenson, D. J.: 1984, in: Gehrels, T., and Matthews, M. S. (eds.), *Saturn*, University of Arizona Press, Tucson, pp. 671–759.
Jones, D.: 1976, *Nature* **260**, 686–689.
Kaiser, M. L.: 1989, in: Tsurutani, B. T., and Oya, H. (eds.), *Plasma Waves and Instabilities at Comets and Magnetospheres*, AGU Monograph **53**, American Geophysics Union, Washington, DC, pp. 221–237.
Kaiser, M. L., and Desch, M. D.: 1982, *J. Geophys. Res.* **87**, 4555–4559.
Kaiser, M. L., Desch, M. D., and Lecacheux, A.: 1981, *Nature* **292**, 731–733.
Kaiser, M. L., Connerney, J. E. P., and Desch, M. D.: 1983, *Nature* **303**, 50–53.

Kaiser, M. L., Desch, M. D., Kurth, W. S., Lecacheux, A., Genova, F., Pedersen, B. M., and Evans, D. R.: 1984a, in: Gehrels, T. and Matthews, M. S. (eds.), *Saturn*, University of Arizona Press, Tucson, pp. 378–415.

Kaiser, M. L., Desch, M. D., and Connerney, J. E. P.: 1984b, *J. Geophys. Res.* **89**, 2371–2376.

Kaiser, M. L., Zarka, P., Desch, M. D., and Farrell, W. M.: 1991, *J. Geophys. Res.* **96**, 19,043–19,047.

Kaiser, M. L., Farrell, W. M., Desch, M. D., Hospodarsky, G. B., Kurth, W. S., and Gurnett, D. A.: 2001, in: Rucker, H. O., Kaiser, M. L., and Leblanc, Y. (eds.), *Planetary Radio Emissions V*, Austrian Academy of Sciences Press, Vienna, pp. 41–48.

Kelley, M. C., and Mozer, F. S.: 1972, *J. Geophys. Res.* **77**, 6900–6903.

Kennel, C. F., and Petschek, H. E.: 1966, *J. Geophys. Res.* **71**, 1–28.

Ksanfomality, L. V., Scarf, F. L., and Taylor, W. W. L.: 1983, in: Hunten, D. M., Colin, L., Donahue, T. M., and Moroz, V. I. (eds.), *Venus*, University of Arizona Press, Tucson, pp. 565–603.

Kurth, W. S.: 1992, in: Rucker, H. O., Bauer, S. J., and Kaiser, M. L. (eds.), *Planetary Radio Emissions III*, Austrian Academy of Science, pp. 329–350.

Kurth, W. S., and Gurnett, D. A.: 1991, *J. Geophys. Res.* **96**, 18,977–18,991.

Kurth, W. S., and Zarka, P.: 2001, in: Rucker, H. O., Kaiser, M. L., and Leblanc, Y. (eds.), *Planetary Radio Emissions V*, Austrian Academy of Sciences Press, Vienna, pp. 247–259.

Kurth, W. S., Gurnett, D. A., and Scarf, F. L.: 1981, *Nature* **292**, 742–745.

Kurth, W. S., Strayer, B. D., Gurnett, D. A., and Scarf, F. L.: 1985, *Icarus* **61**, 497–507.

Kurth, W. S., Gurnett, D. A., Roux, A., and Bolton, S. J.: 1997, *Geophys. Res. Lett.* **24**, 2167–2170.

Kurth, W. S., Hospodarsky, G. B., Gurnett, D. A., Kaiser, M. L., Wahlund, J.-E., Roux, A., Canu, P., Zarka, P., and Tokarev, Y.: 2001a, *J. Geophys. Res*. **106**, 30,239–30,252.

Kurth, W. S., Hospodarsky, G. B., Gurnett, D. A., Lecacheux, A., Zarka, P., Desch, M. D., Kaiser, M. L., and Farrell, W. M.: 2001b, in: Rucker, H. O., Kaiser, M. L., and Leblanc, Y. (eds.), *Planetary Radio Emissions V*, Austrian Academy of Sciences Press, Vienna, pp. 15–28.

Kurth, W. S., Gurnett, D. A., Hospodarsky, G. B., Farrell, W. M., Roux, A., Dougherty, M. K., Joy, S. P., Kivelson, M. G., Walker, R. J., Crary, F. J., and Alexander, C. J.: 2002, *Nature* **415**, 991–994.

Ladreiter, H. P., Zarka, P., and Lecacheux, A.: 1994, *Planet. Space Sci.* **42**, 919–931.

Ladreiter, H. P., Zarka, P., Lecacheux, A., Macher, W., Rucker, H. O., Manning, R., Gurnett, D. A., and Kurth, W. S.: 1995, *Radio Sci.* **30**, 1699–1712.

Lammer, H., Tokano, T., Fischer, G., Stumptner, W., Molina-Cuberos, G. J., Schwingenschuh, K., Rucker, H. O.: 2001, *Planet. Space Sci*. **49**, 561–574.

Lecacheux, A.: 2001, in: Rucker, H. O., Kaiser, M. L., and Leblanc, Y. (eds.), *Planetary Radio Emissions V*, Austrian Academy of Sciences Press, Vienna, pp. 1–13.

Lecacheux, A., and Genova, F.: 1983, *J. Geophys. Res.* **88**, 8993–8998.

Lecacheux, A., Galopeau, P., and Aubier, M.: 1997, in: Rucker, H. O., Bauer, S. J., and Lecacheux, A. (eds.), *Planetary Radio Emissions IV*, Austrian Academy of Science Press, Vienna, pp. 313–325.

Lecacheux, A., Kurth, W. S., and Manning, R.: 2001, in: Rucker, H. O., Kaiser, M. L., and Leblanc, Y. (eds.), *Planetary Radio Emissions V*, Austrian Academy of Sciences Press, Vienna, pp. 29–39.

Le Queau, D., Pellat, R., and Roux, A.: 1984, *Phys. Fluids* **27**, 247–265.

Lockwood, G. E. K.: 1963, *Can. J. Phys.* **41**, 190–194.

Louarn, P., Roux, A., De Feraudy, H., Le Queau, D., Andre, M., and Matson, L.: 1990, *J. Geophys. Res.* **95**, 5983–5995.

Matson *et al.*, this issue.

Mendis, D. A., Hill, J. R., Ip, W.-H., Goertz, C. K., and Grün, E.: 1984, in: Gehrels, T. and Matthews, M. S. (eds.), *Saturn*, University of Arizona Press, Tucson, pp. 546–589.

Meyer-Vernet, N. and Perche, C.: 1989, *J. Geophys. Res.* **94**, 2405–2415.

Meyer-Vernet, N., Aubier, M. G., and Pedersen, B. M.: 1986, *Geophys. Res. Lett.* **13**, 617–620.

Meyer-Vernet, N., Lecacheux, A., and Pedersen, B. M.: 1996, *Icarus* **123**, 113–128.

Miller, S. L.: 1955, *J. Amer. Chem. Soc.* **77**, 2351–2361.
Mott-Smith, H. M., and Langmuir, I.: 1926, *Phys. Rev.* **28**, 727–762.
Neubauer, F. M.: 1980, *J. Geophys. Res.* **85**, 1171–1178.
Neubauer, F. M., Gurnett, D. A., Scudder, J. D., and Hartle, R. E.: 1984, in: Gehrels, T., and Matthews, M. S. (eds.), *Saturn*, University of Arizona Press, Tucson, pp. 760–787.
Oberc, P., and Parzydlo, W.: 1992, *Icarus* **98**, 195–206.
Pedersen, B. M., Meyer-Vernet, N., Aubier, M. G., and Zarka, P.: 1991, *J. Geophys. Res.* **96**, 19,187–19,196.
Prinn, R. G., and Owen, T.: 1976, in *Jupiter*, Gehrels, T. (ed.), University of Arizona Press, Tucson, 319–371.
Prinn, R. G., Larson, H. P., Caldwell, J. J., and Gautier D.: 1984, in: Gehrels, T., and Matthews, M. S. (eds.), *Saturn*, University of Arizona Press, Tucson, pp. 88–149.
Reiner, M. J., Fainberg, J., and Stone, R. G.: 1993, *Geophys. Res. Lett.* **20**, 321–324.
Rucker, H. O., Macher, W., Manning, R., and Ladreiter, H. P.: 1996, *Radio Science* **31**, 1299–1311.
Russell, C. T.: 1991, *Space Science Rev.* **55**, 317–356.
Sagan, C., and Khare, B. N.: 1971, *Astrophys. J.* **168**, 563–569.
Scarf, F. L., and Gurnett, D. A.: 1977, *Space Sci. Rev.* **21**, 289–308.
Scarf, F. L., Gurnett, D. A., and Kurth, W. S.: 1979, *Science* **204**, 991–995.
Scarf, F. L., Gurnett, D. A., Kurth, W. S., and Poynter, R. L.: 1982, *Science,* **215,** 587–594.
Scarf, F. L., Frank, L. A., Gurnett, D. A., Lanzerotti, L. J., Lazarus, A., and Sittler, Jr., E. C.: 1984, in: Gehrels, T. and Matthews, M. S. (eds.), *Saturn*, University of Arizona Press, Tucson, pp. 318–353.
Smith, B. A., *et al.*: 1981, *Science* **212,** 163–190.
Southwood, D., *et al.*, this issue.
Stix, T.: 1992, *Waves in Plasmas, American Institute of Physics*, New York, 6.
Stone, R. G., Bougeret, J. L., Caldwell, J., Canu, P., DeConchy, Y., Cornilleau-Wehrlin, N., Desch, M. D., Fainberg, J., Goetz, K., Goldstein, M. L., Harvey, C. C., Hoang, S., Howard, R., Kaiser, M. L., Kellogg, P. J., Klein, B., Knoll, R., Lecacheux, A., Lengyel-Frey, D., MacDowall, R. J., Manning, R., Meetre, C. A., Meyer, A., Monge, N., Monson, S., Nicol, G., Reiner, M. J., Steinberg, J.-L., Torres, E., deVilledary, C., Wouters, F., and Zarka, P.: 1992, *Astron. Astrophys. Supp. Ser.* **92**, 291–316.
Trauger, J. T., Clarke, J. T., Ballester, G. E., Evans, R. W., Burrows, C. J., Crisp, D., Gallagher, J. S., Griffiths, R. E., Hester, J. J., Hoessel, J. G., Holtzman, J. A., Krist, J. E., Mould, J. R., Sahai, R., Scowen, P. A., Stapelfeldt, K. R., Watson, A. M.: 1998, *J. Geophys. Res.* **103**, 20,237–20,244.
Trotignon, J. G., Beghin, C., Grard, R., Pedersen, A., Formisano, V., Mogilevsky, M., and Mikhailov, Y.: 1987, *Astron. Astrophys.* **187**, 83–88.
Uman, M. A.: 1987, *The Lightning Discharge,* Academic Press, N. York.
Vogl, D. F., Ladreiter, H. P., Zarka, P., Rucker, H. O., Macher, W., Kurth, W. S., Gurnett, D. A., and Fischer, G.: 2001, in: Rucker, H. O., Kaiser, M. L., and Leblanc, Y. (eds.), *Planetary Radio Emissions V*, Austrian Academy of Sciences Press, Vienna, pp. 357–365.
Wahlund, J.-E., Eriksson, A. I., Holback, B., Boehm, M. H., Bonnell, J., Kintner, P. M., Seyler, C. E., Clemmons, J. H., Eliason, J. L., Knudsen, D. J., Norqvist, P., and Zanetti, L. J.: 1998, *J. Geophys. Res.* **103**, 4343–4375.
Warwick, J. W., Pearce, J. B., Peltzer, R. G., and Riddle, A. C.: 1977, *Space Sci. Rev.* **21**, 309–327.
Warwick, J. W., Pearce, J. B., Evans, D. R., Carr, T. D., Schauble, J. J., Alexander, J. K., Kaiser, M. L., Desch, M. D., Pedersen, B. M., Lecacheux, A., Daigne, G., Boischot, A., and Barrow, C. W.: 1981, *Science* **212**, 239–243.
Warwick, J. W., Pearce, J. B., Evans, D. R., Romig, J. H., Alexander, J. K., Desch, M. D., Kaiser, M. L., Aubier, M., Leblanc, Y., Lecacheux, A., and Pedersen, B. M.: 1982, *Science* **215**, 582–687.
Whalström, M. K., Johansson, E., Veszelei, E., Bennich, P., Olsson, M., and Hogmark, S.: 1992, *Thin Solid Films* **220**, 315–320.

Wu, C. S., and Lee, L. C.: 1979, *Astrophys. J.* **230**, 621–626.
Zarka, P.: 1985a, *Icarus* **61**, 508–520.
Zarka, P.: 1985b, in: Rucker, H. O. and Bauer, S. J. (eds.), *Planetary Radio Emissions,* Austrian Academy of Science, Vienna, pp. 237–270.
Zarka. P.: 1998, *J. Geophys. Res.* **103**, 20,159–20,164.
Zarka, P., and Cecconi, B.: 2002, *J. Geophys. Res*., in preparation.
Zarka, P., and Pedersen, B. M.: 1983, *J. Geophys. Res.*, **88**, 9007–9018.
Zarka, P., and Pedersen, B. M.: 1986, *Nature* **323**, 606–608.
Zarka, P., Pedersen, B. M., Lecacheux, A., Kaiser, M. L., Desch, M. D., Farrell, W. M., and Kurth, W. S.: 1995, in *Neptune and Triton,* Cruikshank, D. P. (ed.), University of Arizona Press, 341–387.